



HAL
open science

Assessing Superspheroids in Modeling the Scattering Matrices of Dust Aerosols

Wushao Lin, Lei Bi, Oleg Dubovik

► **To cite this version:**

Wushao Lin, Lei Bi, Oleg Dubovik. Assessing Superspheroids in Modeling the Scattering Matrices of Dust Aerosols. *Journal of Geophysical Research: Atmospheres*, 2018, 123, pp.13,917-13,943. 10.1029/2018JD029464 . insu-03686249

HAL Id: insu-03686249

<https://insu.hal.science/insu-03686249>

Submitted on 2 Jun 2022

HAL is a multi-disciplinary open access archive for the deposit and dissemination of scientific research documents, whether they are published or not. The documents may come from teaching and research institutions in France or abroad, or from public or private research centers.

L'archive ouverte pluridisciplinaire **HAL**, est destinée au dépôt et à la diffusion de documents scientifiques de niveau recherche, publiés ou non, émanant des établissements d'enseignement et de recherche français ou étrangers, des laboratoires publics ou privés.

Copyright

RESEARCH ARTICLE

10.1029/2018JD029464

Key Points:

- Superspheroids were used to model dust aerosols' scattering matrices, and comprehensive comparisons between scattering matrix simulations and measurements were conducted for 25 samples from the Amsterdam-Granada Light Scattering Database
- Superspheroids were shown to be superior to spheroids in reproducing the measurements and show much better performances in concurrently matching the phase function and polarization characteristics at 441.6 and 632.8 nm
- Superspheroids with constrained roundness parameter appear to be highly promising for dust radiative transfer simulations

Correspondence to:

 L. Bi,
bilei@zju.edu.cn

Citation:

 Lin, W., Bi, L., & Dubovik, O. (2018).
Assessing superspheroids in modeling
the scattering matrices of dust aerosols.
*Journal of Geophysical Research:
Atmospheres*, 123, 13,917–13,943.
<https://doi.org/10.1029/2018JD029464>

Received 9 AUG 2018

Accepted 28 NOV 2018

Accepted article online 6 DEC 2018

Published online 27 DEC 2018

Author Contributions:

Conceptualization: Lei Bi**Funding acquisition:** Lei Bi**Investigation:** Wushao Lin**Methodology:** Lei Bi**Supervision:** Lei Bi, Oleg Dubovik**Visualization:** Wushao Lin**Writing - original draft:** Wushao Lin**Writing - review & editing:** Lei Bi, Oleg Dubovik

Assessing Superspheroids in Modeling the Scattering Matrices of Dust Aerosols

 Wushao Lin¹ , Lei Bi¹ , and Oleg Dubovik² 
¹Department of Atmospheric Sciences, School of Earth Sciences, Zhejiang University, Hangzhou, China, ²Laboratoire d'Optique Atmosphérique, UMR 8518, CNRS–Université Lille 1, Villeneuve d'Ascq, France

Abstract Atmospheric dust particles are known to have diverse and irregular morphologies. In order to account for nonsphericity, the spheroidal model with an aspect ratio distribution has been extensively used for modeling the optical properties of dust. The spheroidal model is superior to the spherical shape assumption, but it requires further improvement. In this study, superspheroids' modeling capabilities were systematically examined by comprehensively comparing the spheroid's and superspheroid's scattering matrices. Superspheroids have one more degree of freedom than spheroids and can be nonspherical at an aspect ratio of unity. The invariant imbedding T-matrix and the improved geometrical optics methods were employed to compute superspheroids' single-scattering properties with a wide distribution of aspect ratios and a number of roundness parameters. We then assessed the spheroidal and superspheroidal models' applicability for simulating the scattering matrices of 25 dust samples from the Amsterdam-Granada Light Scattering Database. It was found that extreme aspect ratios for spheroids in reproducing the measurements were unnecessary if superspheroids were used. Even with equi-probable aspect ratio distribution, superspheroids with constrained roundness parameters (from 2.4 to 3.0) could achieve better performances in concurrently matching six nonzero scattering matrix elements from the laboratory measurements. Moreover, superspheroids demonstrated better performances than spheroids in achieving spectral consistency for modeling dust scattering matrices. Therefore, superspheroids appear to be highly promising for atmospheric radiative transfer and remote sensing applications.

1. Introduction

Dust is one of the major constituents of natural atmospheric aerosols and generally originates in arid and semiarid regions (Andreae, 1995; Chiapello et al., 1999; D'Almeida et al., 1991; Ginoux et al., 2001). Small-sized dust particles can travel over a long distance and spread over globally via the synergetic effect of convection currents and general circulation systems (Arimoto, 2001; Ginoux et al., 2004; Prospero et al., 2002; Tegen & Fung, 1994). For this reason, dust aerosols profoundly affect not only regional but also global climates via their direct and indirect influences on radiative forcing (Haywood & Boucher, 2000; Haywood et al., 2001; Kaufman et al., 2002; Konare et al., 2008; Ramanathan et al., 2001; Tegen et al., 1996). Because dust particles have complex geometries and multiple compositions (Haywood et al., 2003; Kaufman et al., 2001), large uncertainties exist as to how to represent dust aerosols when quantifying dust aerosols' single-scattering properties for radiative flux calculations and remote sensing applications. Although significant research efforts have been made in this direction owing to theoretical and computational progress on light scattering by nonspherical and inhomogeneous particles, a challenge remains with respect to dust aerosol optical modeling with development of simplified yet effective dust models for improving atmospheric radiative transfer and remote sensing applications.

As can be seen from dust scanning electron microscopy images (Gao & Anderson, 2001; Muñoz et al., 2001; Okada et al., 2001; Reid et al., 2003), dust particle morphology is nonspherical and exclusively irregular without any preferable morphologies. Thus, the freedom of the aerosol model plays a fundamental role in dust optical modeling. The simplest model uses spherical approximation (one freedom such as particle size), which is commonly used in climate studies. However, numerous studies have shown that spherical approximation oversimplifies the physical process; thus, this may lead to incorrect results or large errors in dust aerosols modeling and then in downward radiative transfer calculations (Feng et al., 2009; Kahnert et al., 2005, 2007; Kalashnikova & Sokolik, 2004; Mishchenko et al., 1997; Yang et al., 2000, 2007). Therefore, as one of the main error sources, it has been well recognized that nonspherical morphology must be considered

when quantifying dust aerosols' radiative effect (Kahnert & Nousiainen, 2006; Kahnert et al., 2005, 2007). The relative importance of treating the dust nonsphericity in climate models and remote sensing applications has been addressed in Mishchenko et al. (1995, 2003). For most practical studies, the spheroidal model, which has one more shape parameter (an aspect ratio) than a sphere, is often employed either in analyzing laboratory measurements of dust samples or for relevant remote sensing applications (Dubovik et al., 2002, 2006; Huang et al., 2015; Mishchenko et al., 1997; Nousiainen & Vermeulen, 2003; Nousiainen et al., 2011). Specifically, a mixture of spheroids with an aspect ratio distribution is employed to compute dust particles' phase matrices. Merikallio et al. (2011) carried out a comprehensive study of spheroids in optical modeling of mineral dusts and recommended a power law shape distribution for reproducing measurements. Apart from spheroids, many other aerosol models, including the Gaussian random particle (Muinonen et al., 1996; Veihelmann et al., 2006), triaxial ellipsoid (Bi et al., 2009), nonsymmetric hexahedra (Bi et al., 2010), agglomerate debris (Zubko et al., 2013), and fractal polyhedral (Jin et al., 2016; Liu et al., 2013) models, have been developed to improve dust optical modeling. Until now, there has not been a standard or a consistent approach for dust optical modeling, and persistent research efforts have been devoted to developing realistic or simplified dust models (see reviews in Nousiainen, 2009, and Kahnert et al., 2014).

To the best of our knowledge, the spheroidal model has been the most frequently used model, although spheroids are idealistic shapes. The fundamental reason is not only due to the model simplicity but also due to its applicability performances, for example, in the retrieval applications associated with the Aerosol Robotic Network (Dubovik et al., 2006), Moderate Resolution Imaging Spectroradiometer (Levy, Remer, & Dubovik, 2007; Levy, Remer, Mattoo, et al., 2007), Total Ozone Mapping Spectrometer (Sinyuk et al., 2003), Spinning Enhanced Visible and Infrared Imager (Govaerts et al., 2010; Wagner et al., 2010), Polarization and Anisotropy of Reflectances for Atmospheric Science coupled with Observations from a Lidar (Dubovik et al., 2011), and others (e.g., Li et al., 2006; Veselovskii et al., 2010). However, the community has been well aware of the spheroidal model's limitations, such as the inconsistency in matching phase function and polarization characteristics of dust (e.g., Nousiainen, 2009). Some potential issues were identified with the phase function over large scattering angles and the magnitudes of polarization and depolarization characteristics.

The aim of this paper was to improve the spheroidal model by investigating superspheroids in modeling dust optical properties, following a logical development from spheres to spheroids, and then to superspheroids. Superspheroids are considered a generalization of spheroids (see section 2 for details). For simplicity, we only consider superspheroids with one roundness parameter. Even with this simplified treatment, a variety of shapes can be generated to model the aspect ratio, roundness, and concavities. The motivation of this study was twofold. First, we intended to study whether superspheroids can improve the current spheroid-based modeling. The enlarged shape space permits an optimal choice to constrain the morphological parameters. Second, we asked if it is possible to build a general framework of model particles with a single equation, which can be more flexible in modeling various nonspherical aerosol particles. Such a rationale also follows the most recent study concerning sea salts' optical properties (Bi, Lin, Wang, et al., 2018), which uses a branch of superellipsoids to model sea-salt aerosols. Furthermore, the superspheroidal model is expected to be promising, because it also retains the rule of simplicity when building aerosol models. It should be noted that the above described study (with superspheroids) requires much more computational time in comparison with the spheroidal model. However, recent advances in computational techniques permit such a study with reasonable computational resources. Specifically, we employed the invariant imbedding T-matrix (Bi & Yang, 2014; Bi et al., 2013a, 2013b) and the improved geometric optics methods (II-TM and IGOM, respectively; Bi et al., 2009; Yang & Liou, 1996; Yang et al., 2007) for computing the single-scattering properties of superspheroidal particles. We first investigated the way in which scattering matrix elements of superspheroids change with respect to aspect ratio and roundness parameter. The results were compared with their spheroid counterparts (spheres as a special case) to give an understanding of the overall performance of the spheroidal and superspheroidal models. We then assessed the applicability of the two models by comparing theoretical results with the measured scattering matrices from the Amsterdam-Granada Light Scattering Database (Muñoz et al., 2000, 2004, 2012; Volten et al., 2000, 2006, 2007). Specifically, 25 aerosol samples were studied in order to obtain a comprehensive understanding of superspheroid modeling capabilities. In section 2, we briefly introduce the superspheroidal model. Representative results are then discussed in section 3. The summary and conclusions of this study are given in section 4.

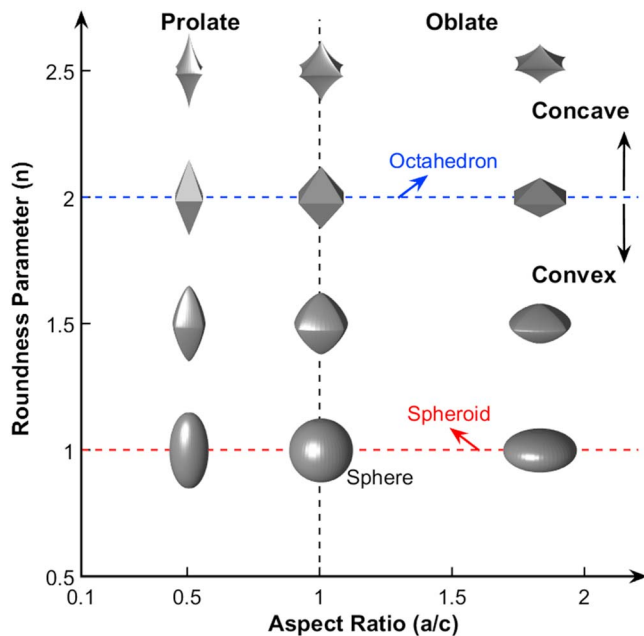


Figure 1. Shape variation in a superspheroidal particle space.

2. Model and Computational Methods

2.1. Spheroidal and Superspheroidal Models

Particles with identical or close aspect ratios can have diverse shapes. Particularly, particles with a unity aspect ratio can be irregular (Gao & Anderson, 2001; Liu et al., 2018; Muñoz et al., 2001; Okada et al., 2001; Reid et al., 2003). The fact that the spheroid with a unity aspect ratio is a sphere makes it preferable to use large aspect ratios in modeling dust optical properties. In this study, we enlarged the shape space of model particles to represent dust aerosols by using the superellipsoidal equation, shown in the following (Barr, 1981):

$$\left[\left(\frac{x}{a} \right)^{2/e} + \left(\frac{y}{b} \right)^{2/e} \right]^{e/n} + \left[\frac{z}{c} \right]^{2/n} = 1, \quad (1)$$

in which a , b , and c are the three semiaxes of a superellipsoid particle along the x , y , and z directions in the Cartesian coordinate system. In the equation, the parameters e and n are defined as roundness parameters, which determine the morphological variation of the particle with fixed aspect ratios (a/c and b/c). To simplify the model without losing diversity, we opted to focus on superellipsoids with $a = b$ and $e = n > 1.0$. Equation (1) can then be simplified to the following form:

$$\left(\frac{x}{a} \right)^{2/n} + \left(\frac{y}{a} \right)^{2/n} + \left(\frac{z}{c} \right)^{2/n} = 1. \quad (2)$$

Hereafter, the superspheroidal shape was only determined by the aspect ratio a/c and the roundness parameter n ; $a/c < 1$ for prolate particles, and $a/c > 1$ for oblate particles. The size parameter can be defined as kx_m , in which k is the wave number ($k = 2\pi/\lambda$, λ is the wavelength), x_m is the maximum of semiaxes, indicating that $x_m = c$ for prolate particles and $x_m = a$ for oblate particles.

The superiority of the superellipsoidal model can be found in the fact that it contains abundant shapes, and the shape variation is continuous, which permits flexibility in constraining the morphological parameters in relevant remote sensing or climate modeling studies. As shown in Figure 1, when $n = 1.0$, the shape exists as a spheroidal particle, and specifically, a spherical particle when $a/c = 1.0$. It can be seen that as n increases, the shape becomes octahedron-like, and a perfect octahedron is formed at $n = 2.0$. For $n > 2.0$, the octahedron becomes concave and shows sharp edges. It should be noted that another branch of superellipsoids ($n < 1$; not shown here) was employed in the study by Bi, Lin, Liu, et al. (2018) and Bi, Lin, Wang, et al. (2018) to model cube-like sea-salt aerosols.

The advantage of superspheroids can be understood in another way. The aspect ratio, volume, and projected area are important microphysical particle properties that significantly impact a superspheroid's optical properties. By considering the particle as composed of a number of dipoles (Bohren & Huffman, 1983), the aspect ratio is considered as a simplified variable used to describe dipole distribution, and the particle volume determines the total number of dipoles. For relatively large particles, the projected area fundamentally determines the diffraction and extinction cross section (van de Hulst, 1981). Therefore, for a given nonspherical particle, it is expected to concurrently match the aspect ratio, volume, and average projected area by using a model particle. However, it is almost impossible to meet such requirement based on the spheroidal model. If a superspheroidal model is applied, this problem can be solved. This idea suggests that for a given aerosol particle, it is possible to identify a superspheroid that can concurrently match both the surface area and the volume with an identical or close aspect ratio. In reality, the aerosols are a mixture of different particle shapes rather than a single particle. However, the aforementioned advantage of superspheroids allows for much more flexibility in modeling dust aerosols' optical properties than do spheroids.

2.2. Computational Methods

The first use of superellipsoids in light-scattering computations can be found in Wriedt (2002) by using discrete sources method. Here a combination of the II-TM and IGOM methods was used for calculations.

The II-TM was applied to particles with small-to-moderate size parameters, and the IGOM was used for those with larger size parameters. The theoretical framework and details of the computational program have been described by Bi et al., 2013a, 2013b, and Bi and Yang, 2014. The calculations were carried out for a variety of superspheroids with an aspect ratio ranging from 0.5 to 2.0 and a roundness parameter ranging from 1.0 to 3.0. In total, 11 aspect ratios and 11 roundness parameters (note that $n = e = 1.0$ for spheroids) were selected for calculations. In practice, a threshold size parameter should be determined by merging the II-TM and IGOM computations. Based on a few test cases, we found that the use of IGOM at a size parameter >40.0 was sufficient to determine the accuracy of the bulk scattering matrix, which is an integral of the scattering matrix over a size distribution. Thus, the II-TM was applied to the computation of the single-scattering properties of superspheroids with a size parameter ≤ 40.0 , and the IGOM was applied to size parameter >40.0 . Results justifying the aforesaid choice and the computational time will be illustrated in section 3.1. For spheroids, the II-TM was used when the size parameter was <100.0 , and the IGOM was applied to size parameter >100.0 . Computations were carried out for a size parameter range of $[0.1, 1000]$.

2.3. Bulk Scattering Matrix

The bulk scattering matrix determines the relationship between the Stokes vector of the incident beam and that of the scattered beam. The Stokes vector contains four components $[I, Q, U, V]$. The first parameter I gives the intensity of light beam. Q , U , and V describe the linear and circular polarization of the beam. The 4×4 scattering matrix is described below (Bohren & Huffman, 1983):

$$\begin{pmatrix} I(\theta) \\ Q(\theta) \\ U(\theta) \\ V(\theta) \end{pmatrix}_{sca} = \left(\frac{1}{kR}\right)^2 \begin{pmatrix} P_{11}(\theta) & P_{12}(\theta) & P_{13}(\theta) & P_{14}(\theta) \\ P_{21}(\theta) & P_{22}(\theta) & P_{23}(\theta) & P_{24}(\theta) \\ P_{31}(\theta) & P_{32}(\theta) & P_{33}(\theta) & P_{34}(\theta) \\ P_{41}(\theta) & P_{42}(\theta) & P_{43}(\theta) & P_{44}(\theta) \end{pmatrix} \begin{pmatrix} I \\ Q \\ U \\ V \end{pmatrix}_{inc}, \quad (3)$$

in which R is the distance between the scatterer and the detector and θ is the scattering angle. For randomly oriented superspheroidal particles (note that superspheroids have a plane of symmetry), the scattering matrix has only six independent elements and thus can be simplified as

$$\mathbf{P} = \begin{pmatrix} P_{11}(\theta) & P_{12}(\theta) & 0 & 0 \\ P_{12}(\theta) & P_{22}(\theta) & 0 & 0 \\ 0 & 0 & P_{33}(\theta) & -P_{43}(\theta) \\ 0 & 0 & P_{43}(\theta) & P_{44}(\theta) \end{pmatrix}. \quad (4)$$

The definition of random orientation is consistent with that given by Mishchenko and Yurkin (2017). In equation (4), the phase function P_{11} is normalized according to the equation:

$$\frac{1}{2} \int_0^\pi P_{11}(\theta) \cos\theta d\theta = 1. \quad (5)$$

In laboratory measurements, the phase functions are only obtained for a limited range of scattering angles. Thus, instead of equation (5), the phase functions are sometimes normalized at a particular scattering angle (such as 30° in a study by Muñoz et al. (2012)). For comparing theoretical simulations and measurements, theoretical phase functions are also normalized at the scattering angle of 30° .

The bulk scattering matrix can be obtained by integral over a size distribution:

$$\langle P_{ij} \rangle = \frac{\int_0^\infty P_{ij}(r) C_{sca}(r) \frac{dN}{dr} dr}{\langle b_{sca} \rangle}, \quad (6)$$

in which P_{ij} represents an arbitrary element in equation (4); C_{sca} is the scattering cross section; $\langle b_{sca} \rangle$ is the scattering coefficient; and dN/dr is the size distribution. For theoretical studies, the lognormal size distribution is often employed:

$$\frac{dN}{d \ln r} = \frac{N_0}{\sqrt{2\pi} \ln \sigma} \exp \left[-\frac{(\ln r - \ln r_m)^2}{2(\ln \sigma)^2} \right], \quad (7)$$

where N_0 is the number of particles per volume, r_m is the mean radius, and σ is the standard deviation. In this study, the particle size is defined as the radius of projected-area-equivalent sphere. The projected area size distribution for specific aerosol samples can also be obtained from diffraction measurements. In the Amsterdam-Granada Light Scattering Database (Muñoz et al., 2012), the projected area size distribution was measured by using a Fritsch laser particle sizer that employs the Fraunhofer diffraction theory for spheres. Either theoretical size distribution or measured data have been used in studies in the literature according to various study perspectives.

3. Results

3.1. Computational Accuracy and Time

The IGOM accuracy was systematically examined in previous studies (Bi & Yang, 2014; Bi et al., 2009; Yang et al., 2007) for a number of particle shapes including ellipsoids and ice crystals. Here Figure 2 (columns 1–3) shows a typical example of comparing the phase matrix elements of superspheroids computed from the II-TM and IGOM at three size parameters (20, 40, and 50). As expected, the IGOM accuracy improves as the size parameter increases. As mentioned in section 2.2, a threshold size parameter should be determined for merging the II-TM (at small-to-moderate size parameters) and IGOM (at large size parameters) computations. To estimate the choice of a threshold size parameter on the accuracy of the size-averaged optical properties, the rightmost panel shows the bulk scattering matrix elements obtained by using three numerical schemes (Case 20, Case 40, and Case 50) corresponding to the threshold size parameter of 20.0, 40.0, and 50.0. A lognormal size distribution with a mean radius of 1.9 μm and a geometrical standard deviation of 2.15 was applied. The wavelength was selected to be 441.6 nm. It is found that slight differences exist between the scattering matrix elements of Case 20 and Case 50. The differences between Case 40 and Case 50 are almost indistinguishable. In terms of computation accuracy, it was expected to apply the II-TM for even large size parameters. However, the computational time of the II-TM significantly increases with respect to the size parameter. For example, the time spent on the three size parameters (20, 40, 50) were ~ 5 min, ~ 2.5 hr, and ~ 9 hr by using 24 central processing units. Finally, in considering the IGOM accuracy and affordable computation time, a threshold size parameter of 40 was chosen in all the remaining computations.

3.2. Comparisons of Scattering Matrix Elements Between Spheroids and Superspheroids

For practical applications, a mixture of model particles is usually employed to represent an ensemble of dust aerosols. The scattering matrix is an average of the model particles' phase matrices. As such, the scattering phase matrices for each particle serve as the *basis* functions. Therefore, it is beneficial to first identify superspheroids' optical characteristics with different aspect ratios and roundness parameters. The simulations were carried out at a wavelength of 441.6 nm, and the refractive index was set at $1.50 + i0.001$. In this situation, we used a lognormal size distribution (see equation (7)) to obtain a bulk scattering matrix. The mean radius was 1.9 μm , and the geometrical standard deviation was 2.15, which are the same as the coarse mode dust-like aerosols in the Optical Properties of Aerosols and Clouds (Hess et al., 1998).

Figure 3 shows the six scattering matrix elements of spheroids with different aspect ratios, even though they have been extensively studied in previous studies (Dubovik et al., 2006; Merikallio et al., 2011; Mishchenko et al., 1997; Nousiainen & Vermeulen, 2003). The special case of a sphere is indicated with black dashed curves. As can be seen from the phase function (i.e., P_{11}), spheres have strong backscattering (scattering angle $> 160^\circ$) and low side scattering ($100^\circ < \text{scattering angle} < 150^\circ$). It can be seen that spheroid backscattering becomes weak as the aspect ratio departs from unity, while side scattering becomes strong. As the aspect ratio departs most from unity (such as $a/c = 0.3$ and 3.0), the phase function curves become smooth. Such features can explain why spheroids with extreme aspect ratios are most useful, because the measured phase function of aerosol samples is relatively smooth and flat at nearly backscattering directions (Merikallio et al., 2011). In comparison with a sphere, spheroids also have quite different $-P_{12}/P_{11}$ element. For example, the $-P_{12}/P_{11}$ element for a sphere has a shape peak at $\sim 160^\circ$, which is rarely seen for dust particles. In general, spheroids have higher $-P_{12}/P_{11}$ at scattering angles $< 90^\circ$ and smaller $-P_{12}/P_{11}$ at scattering angles $> 90^\circ$. The P_{22}/P_{11} element determines the model particles' depolarization capability (P_{12} element also has

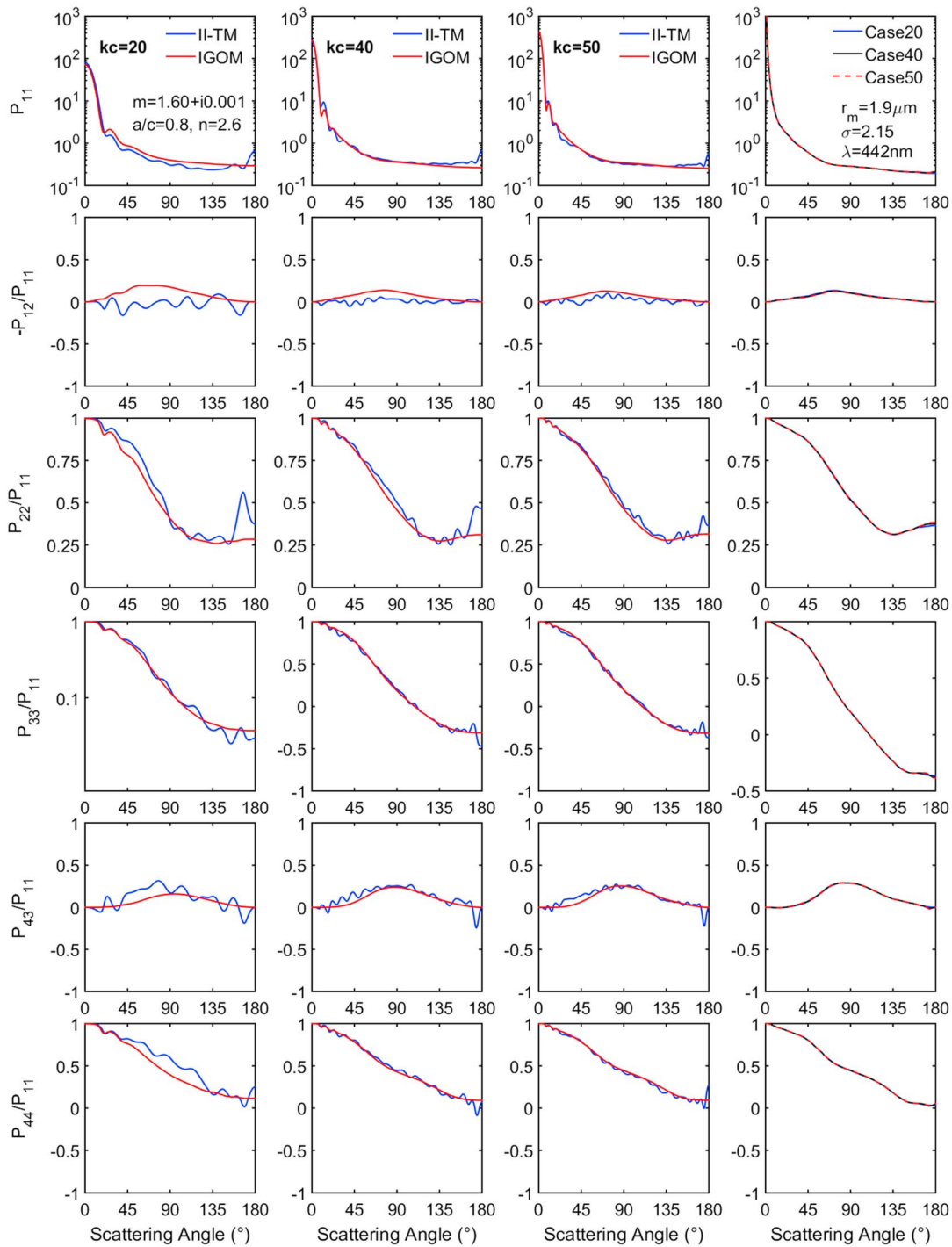


Figure 2. Columns 1–3: comparison of the phase matrix elements computed from the II-TM and IGOM at three different size parameters (i.e., 20, 40, and 50). The rightmost panel: the bulk scattering phase matrix elements obtained by using three numerical schemes (Case 20, Case 40, and Case 50) corresponding to the threshold size of 20.0, 40.0, and 50.0 for merging the II-TM and IGOM computations. A lognormal size distribution with a mean radius of 1.9 μm and a geometrical standard deviation of 2.15 was applied. The wavelength was selected to be 441.6 nm.

impact for side scattering). For spheroids, P_{22}/P_{11} is sensitive to the particle aspect ratio. Readers are referred to a study by Bi, Lin, Liu, et al. (2018) for a systematical study of the depolarization of nonspherical particles in a superellipsoidal shape space. Another interesting feature is that both P_{33}/P_{11} and P_{44}/P_{11} have a peak near the backscattering angle and then quickly drop to -1 at 180° , which was not found for spheroids. Overall, an

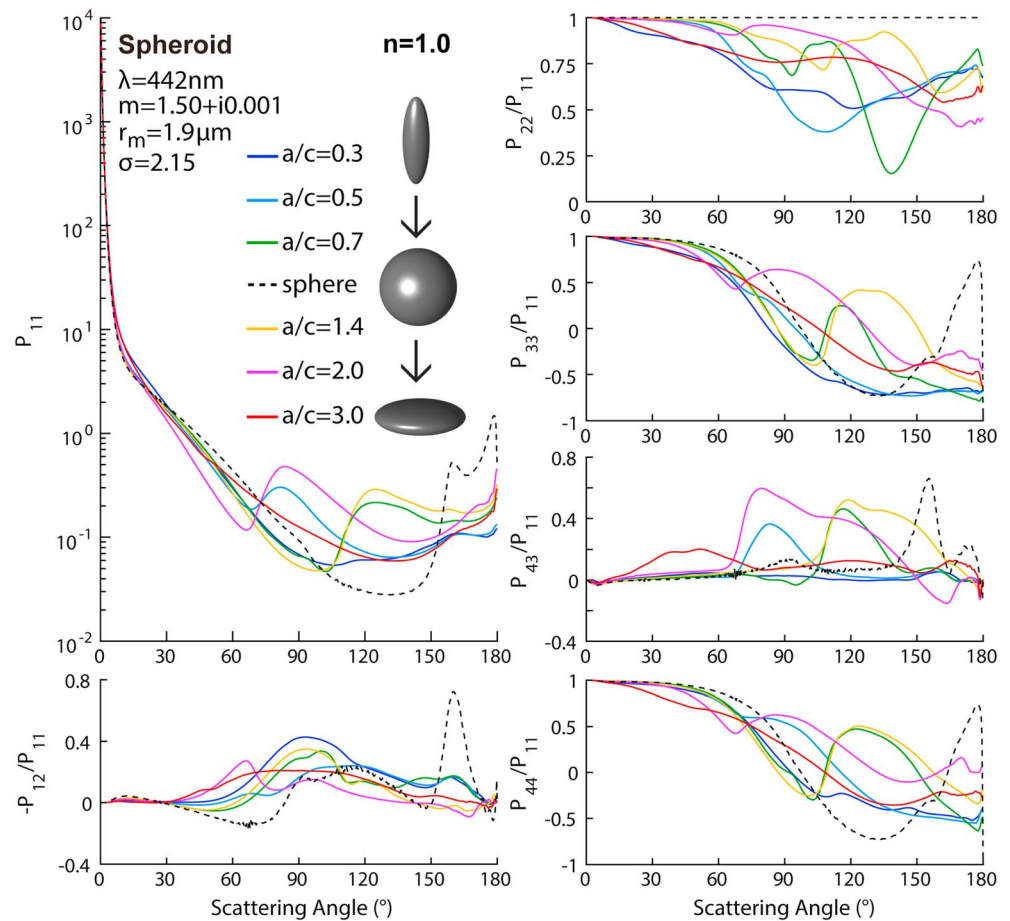


Figure 3. Scattering matrix elements of spheroids with different aspect ratios. The dashed line represents the spheres' results.

obvious characteristic of the scattering matrix elements of spheroids is that curves have strong oscillation structures, which gradually disappear as the aspect ratio becomes extreme. This feature also explains to some extent why extreme aspect ratios (>2.0) have to be used to reproduce the laboratory measurements (e.g., Merikallio et al., 2011).

Figure 4 shows the scattering matrix elements of a set of superspheroids with the same roundness parameter ($n = 2.0$) but with different aspect ratios. In Figure 4, the actual shapes of the superspheroids appear to be octahedral. Similar to the case of spheroids, the backscattering becomes weak as the aspect ratio departs from unity except for the aspect ratio of 0.8. However, strong side scattering observed in Figure 3 was not found for superspheroids. It can be seen that the $-P_{12}/P_{11}$ become more significant and more positive as the aspect ratio departed from unity at large scattering angles ($> \sim 50^\circ$). P_{22}/P_{11} has a minimum value at a scattering angle of around 135° and then peaks near the backscattering angle (except for the aspect ratio of 2.0). In comparison with the case of spheroids (shown in Figure 3), the values of $-P_{12}/P_{11}$ and P_{43}/P_{11} have smaller ranges. The oscillation structures become much weaker for all the six scattering matrix elements.

Figure 5 is similar to Figure 4 except that the roundness parameter is 3.0. In contrast, the scattering matrix elements demonstrated little sensitivity to the aspect ratio. When compared to Figure 4, the oscillation structure almost disappears. Two facts may explain the relative insensitivity to the aspect ratio. First, concave surface structure may have suppressed particular scattering features. Second, although the aspect ratio was quite different, the portion of volume associated with those geometry edges was small (but the point edge part is critical to determine the aspect ratio). Thus, the major bodies of the particles contributing to the scattering appear to be similar. In addition, it was found that high $-P_{12}/P_{11}$ was associated with relatively

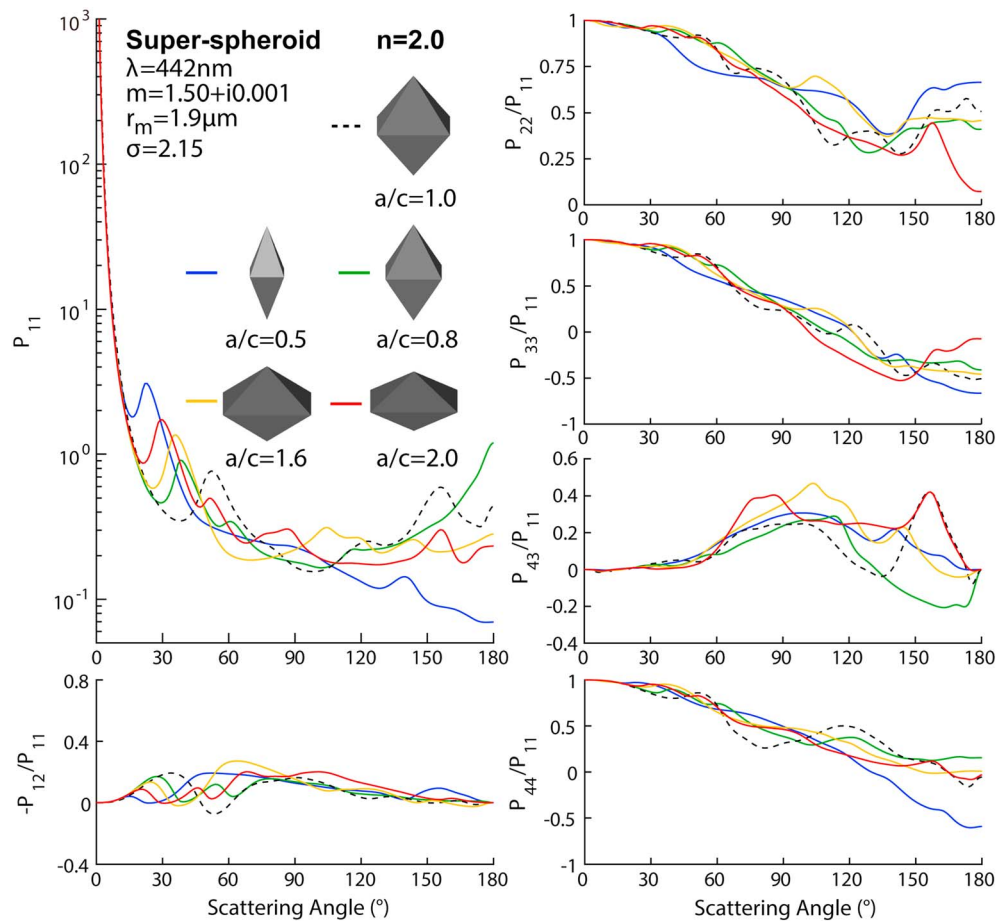


Figure 4. Scattering matrix elements of superellipsoids with different aspect ratios. The roundness parameter is 2.0. The dashed line indicates an aspect ratio of unity.

small volume ($-P_{12}/P_{11} = 1$ at 90° scattering angle for the Rayleigh scattering); this scattering matrix element was positive and relatively high at 90° for most measurements in the Amsterdam-Granada Light Scattering Database (Muñoz et al., 2012). Note that for spheroids, small volumes can be obtained by changing the aspect ratio, while for superspheroids, small volumes can be obtained by increasing the roundness parameter. Therefore, the extreme aspect ratios for spheroids and large roundness parameters of superspheroids tend to produce expected scattering features for $-P_{12}/P_{11}$.

Next, by fixing the aspect ratio, we were able to investigate the change in the scattering matrix elements with respect to the roundness parameter. The shape of the superspheroids varied from a spheroid ($n = 1.0$) to a concave octahedron ($n > 2.0$). Figure 6 shows the scattering matrix elements of spheres and superspheroids with an aspect ratio of unity but with different roundness parameters. It is noteworthy that the superspheroids are seen as nonspherical particles although the aspect ratio is 1.0. The scattering matrix elements of superspheroids with a roundness parameter of 1.2 demonstrate large difference compared to those of spheres, although the superspheroids are seen as nearly spherical. As the roundness parameter increases, the curves can be seen to change to be smooth and featureless. The flat side scattering and backscattering of the phase function was found for large roundness parameters, and P_{22}/P_{11} is shown to decrease in the figure as the roundness parameter increases.

Figure 7 shows the scattering matrix elements of five prolate particles ($a/c = 0.5$) with shapes that change from spheroid to concave octahedron-like superspheroids. The scattering matrix elements of superspheroids, except for those with the roundness parameter of 1.2, demonstrate large differences compared to those of the spheroid. However, it can be seen in the figure that the differences between the concave superspheroids ($n = 2.4$ and $n = 3.0$) are relatively small. An outstanding feature of the spheroidal model (in general) is a phase

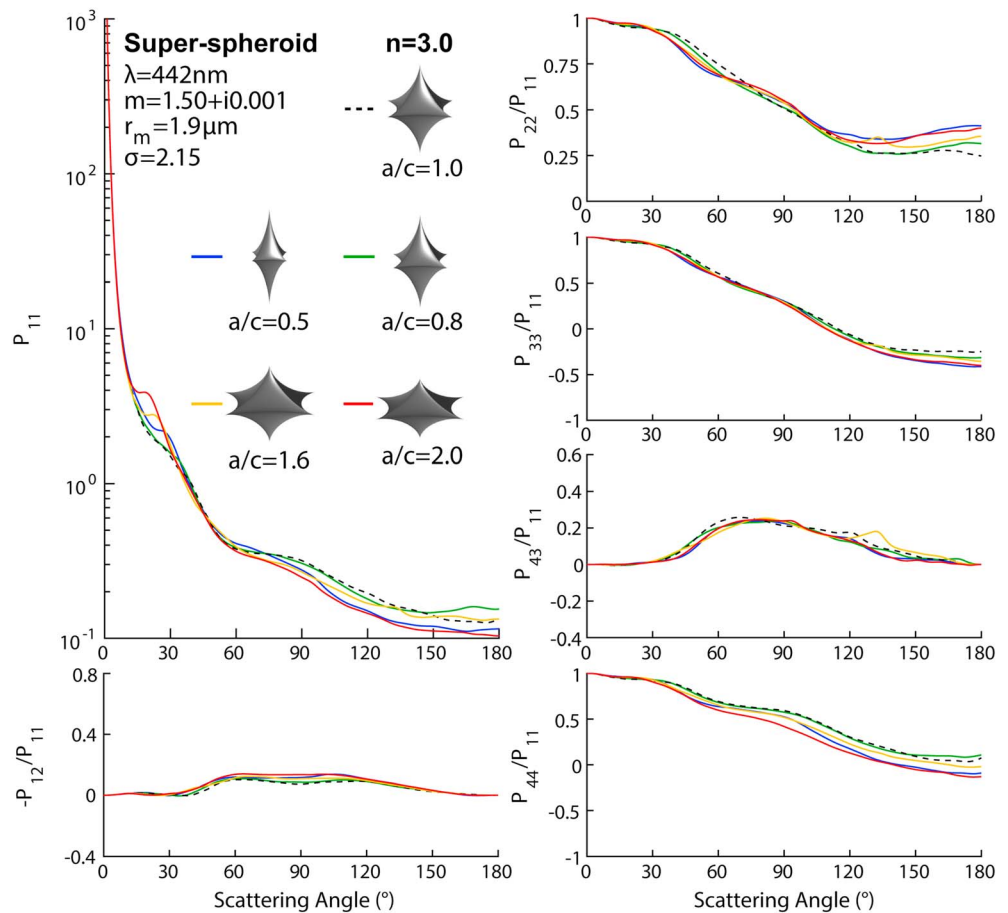


Figure 5. Results are similar to those in Figure 4, but the roundness parameter is 3.0.

function peak at approximately 90°, which is an intrinsic property associated with the geometry. Furthermore, the phase function is usually fairly low between 100 and 150°. Such features are not found with superspheroids. In particular, as the roundness parameter increases, the curves of $-P_{12}/P_{11}$ and P_{43}/P_{11} become relatively smooth and resembled those characteristics of aerosol optical measurements (next section). Thus, as a particle model (similar to a basis function), superspheroids are expected to be a better candidate than spheroids.

The modeling performances in relation to roundness parameter of oblate superspheroids ($a/c = 2.0$) are similar to prolate superspheroids, as presented in Figure 8. However, the scattering matrix elements of the oblate spheroid have quite different characteristics in comparison with those of the prolate spheroid (see Figure 7). For example, the two curves of P_{22}/P_{11} demonstrated the opposite trend as seen in the figure. Again, it can be seen that the features of the scattering matrix elements for spheroids gradually disappear for large roundness parameters.

From the comparisons made in Figures 3–8, it can be seen that the overall patterns of the scattering matrix elements of superspheroids with large roundness parameters demonstrated similarity with those of the measurements, which indicates that the superspheroidal model may be an appropriate model to reproduce the scattering matrices of measurements without using extreme aspect ratios. Note that the minimum and maximum values of the aspect ratios of superspheroids were 0.5 and 2.0, respectively. Comparisons between simulations and the laboratory measurements are presented in section 3.2.

3.3. Comparison Between Simulations and Measurements

Laboratory measurements are an important approach for obtaining characteristics of realistic dust aerosols' scattering matrix properties. A number of experiments that have been conducted have addressed this

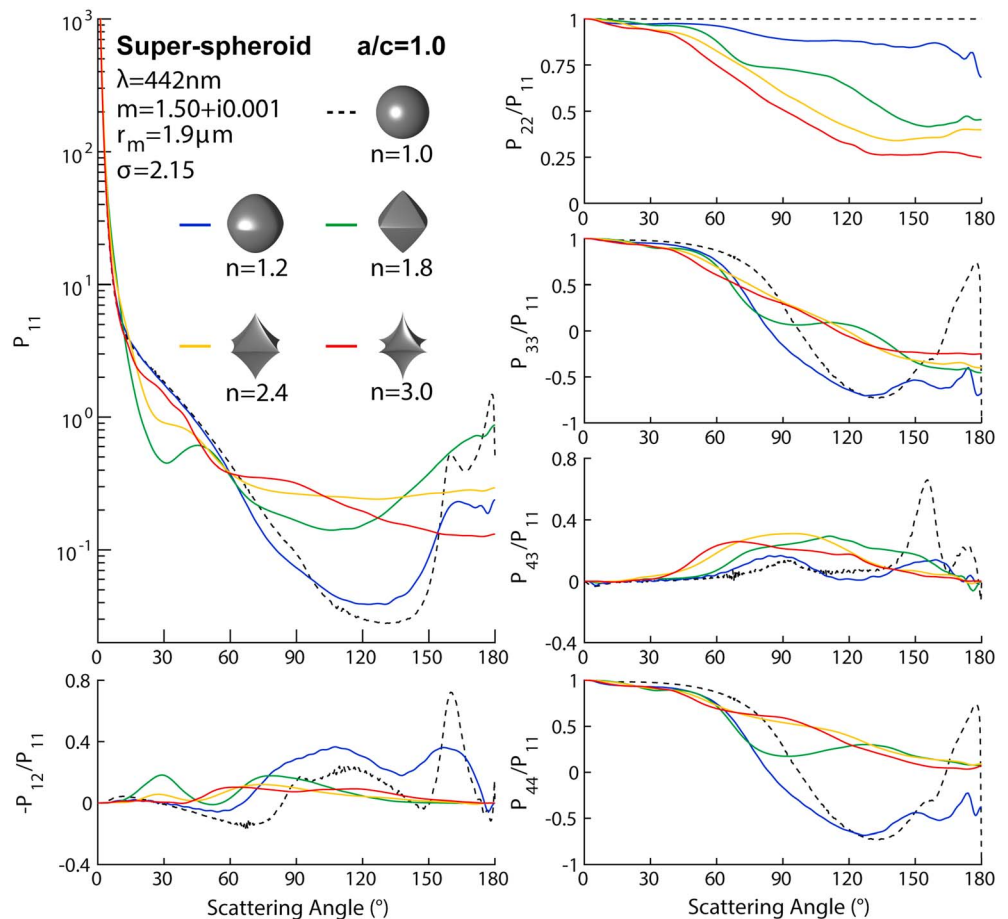


Figure 6. Scattering matrix elements of superspheroids with different roundness parameters and an aspect ratio of 1.0.

subject (e.g., Liu et al., 2018; Muñoz et al., 2012; Volten et al., 2006; Wang et al., 2015). Although the shapes and structures of dust particles were too complicated and differed from region to region, the light scattering property results obtained from experiments may provide a valuable reference for building a dust aerosol model. With improved knowledge of dust models, theoretical approaches can be used to obtain reasonable optical properties of dust aerosols in various application perspectives. Furthermore, experimental approaches can provide information about refractive index, size ranges, and dust particle shapes, all of which are important parameters for simulations. Simulations and experiments can be mutually beneficial and both of them are indispensable.

The superspheroids were divided into several groups according to roundness parameters. In each group, the superspheroids had 11 different aspect ratios (namely, 0.5–1.0 in increments of 0.1 and 1.2–2.0 in increments of 0.2) but with the same roundness parameter. The simulating scattering matrices were compared to the laboratory measurements from the Amsterdam-Granada Light Scattering Database (Muñoz et al., 2000, 2004, 2012; Volten et al., 2000, 2006, 2007). To obtain a comprehensive assessment of how the superspheroidal model performs in modeling the scattering matrices of dust aerosols, comparisons were conducted for a total of 25 samples at both 441.6 and 632.8 nm (if available). The microphysical properties and refractive indices of these samples are given in Table 1. These selected samples are shown to cover a wide range of refractive index and size distribution. Samples that have very large refractive indices such as hematite and rutile or aggregate morphology such as fly ash were not considered in this study. In addition, the Sahara sand from Libya was not considered because its effective radius was too large (124.75 μm). All of the scanning electron microscopy images of different samples were acquired from the database (Muñoz et al., 2012; Volten et al., 2006). To retain the consistency between simulations and measurements as much as possible, the size distribution of each sample we selected for modeling was the same as its measurement counterpart,

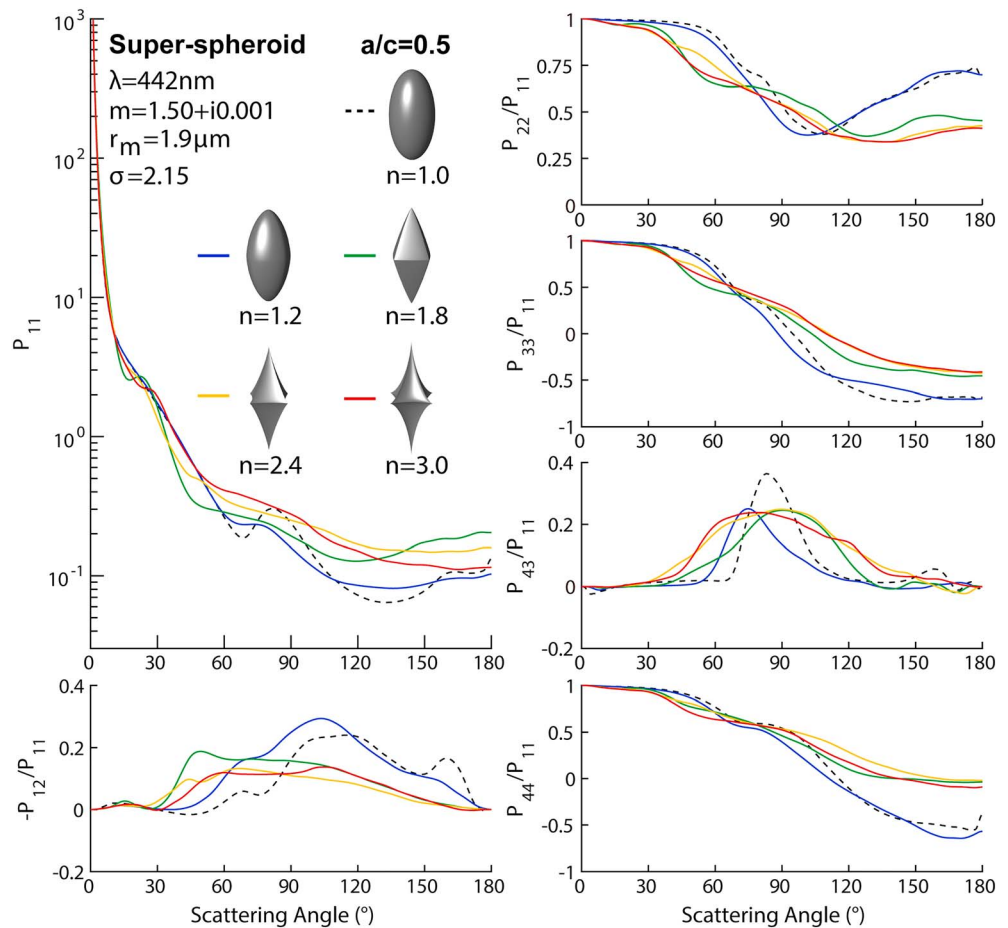


Figure 7. Results are similar to Figure 6, but the aspect ratio is 0.5.

although uncertainties exist. The minimum and maximum size parameters were 0.1 and 1,000, respectively, indicating that the actual size ranges were 0.007–70.3 and 0.01–100.7 μm at 441.6 and 632.8 nm, respectively. Although some particles in the samples had size parameters that exceeded these ranges, their contribution to the scattering matrix elements was negligible. It should be noted that the refractive index of each sample we chose for simulation may have been slightly different from the estimated one suggested by the database.

In traditional studies, an optimal aspect ratio distribution (such as, a power law distribution) is applied to match theoretical simulations based on the spheroidal model with those from measurements, although this shape distribution is most often inconsistent with real distribution values (Chou et al., 2008; Kandler et al., 2011; Okada et al., 2001; Reid et al., 2003). For superspheroids, an optimal shape distribution can also be obtained by following similar procedures. However, the exact shape distribution is usually unknown in most cases. Thus, in this study, an equi-probable distribution of aspect ratio was employed for assessing the modeling capabilities of superspheroids, although it might be unrealistic neither (e.g., Veghte & Freedman, 2014). It should be noted that an equi-probable aspect ratio distribution might be unfair in comparison with spheroids, since it is clear that if one uses spheroids, near-spherical particles should be excluded. For consistency, equi-probable distribution was used for spheroids, because we want to understand how the roundness parameter affects the comparison. The use of power law aspect ratio distribution for spheroids was presented in section 3.3.

3.3.1. Feldspar, Red Clay, and Quartz

Feldspar was the most extensively studied sample. The effective radius was shown to be 1.0 μm , and the effective standard deviation of the radius was 1.0. The real part of the refractive index was estimated to range from 1.50 to 1.60, and the imaginary part ranged from 10^{-5} to 10^{-3} . Figure 9 shows the comparison between simulations and measurements at the wavelength of 632.8 nm. The six nonzero elements (namely, P_{11} , $-P_{12}/$

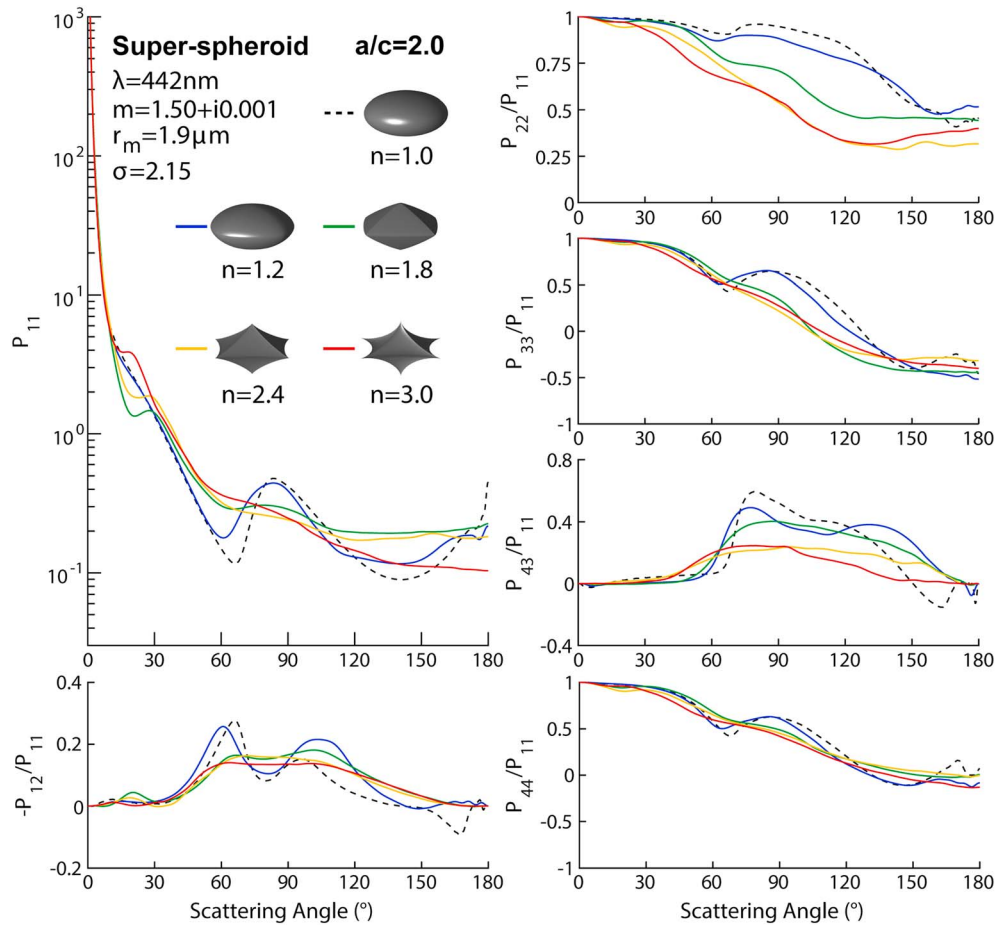


Figure 8. Similar to Figure 6, but the aspect ratio is 2.0.

P_{11} , P_{22}/P_{11} , P_{33}/P_{11} , P_{43}/P_{11} , and P_{44}/P_{11}) were plotted. The refractive index used for simulation was $1.50 + i0.001$. Note that P_{11} was normalized to unity at a fixed scattering angle, namely, 30° . From the figure, we can see that spheroids with an equi-probable shape distribution completely failed to reproduce the measured scattering matrix elements of feldspar. The values of $-P_{12}/P_{11}$ was negative for spheroidal model, while the measured results were positive. Pronounced differences between results of spheroids and measurements were found for P_{22}/P_{11} and P_{43}/P_{11} at scattering angles ranging from 90° to 180° . After considering the aspect ratio distribution, results of superspheroids with roundness parameter of 1.2 were similar to that of the spheroids. That is because these two groups of particles have very close shapes. As the roundness parameter increased, the superspheroids started to demonstrate its superiority in modeling the scattering matrix. Concave particles ($n > 2.0$) appear to be more practical than convex particles ($n < 2.0$) according to the results. As illustrated in Figure 9, simulations with $n = 2.6$ and $n = 3.0$ present similar results with observable differences. In contrast, as seen in the figure, when the roundness parameter changes from 1.2 to 1.8, the particle's volume and surface area changed significantly as the shape of the particle changed from spheroid to octahedron-like. Superspheroids with a roundness parameter of 3.0 can reproduce all six scattering matrix elements with great consistency in the measurements.

The simulated results of the red clay sample and the corresponding measurements at a wavelength of 632.8 nm are presented in Figure 10. In the last panel of the figure, it can be seen that red clay shows a larger effective radius ($1.5 \mu\text{m}$) than feldspar with an effective variance of 1.6. The refractive index used for the simulation was $1.50 + i0.001$. Superspheroids with a roundness parameter of 3.0 can be used to successfully reproduce red clay's measured phase function and $-P_{12}/P_{11}$ (but failed for other elements, especially for P_{44}/P_{11}).

Table 1
Summary of the Samples Investigated in This Study

| Sample | $r_{\text{eff}}/\mu\text{m}$ | v_{eff} | Re (m) | Im (m) |
|--------------------------------|------------------------------|------------------|------------|---------------|
| Allende | 0.8 | 3.3 | 1.65 | 0.001 |
| Feldspar ^a | 1.0 | 1.0 | 1.50–1.60 | 0.001–0.00001 |
| Red clay ^a | 1.5 | 1.6 | 1.50–1.70 | 0.001–0.00001 |
| Green clay ^a | 1.55 | 1.4 | 1.50–1.70 | 0.001–0.00001 |
| Quartz | 2.3 | 2.3 | 1.54 | 0 |
| Martian analog palagonite | 4.5 | 7.3 | 1.50 | 0.001–0.0001 |
| Loess ^a | 3.9 | 2.6 | 1.50–1.70 | 0.001–0.00001 |
| Sahara ^a | 8.2 | 4.0 | 1.50–1.70 | 0.001–0.00001 |
| Forsterite (initial) | 1.8 | 5.4 | 1.63 | 0 |
| Forsterite (small) | 1.3 | 3.1 | 1.63 | 0 |
| Forsterite (washed) | 3.3 | 4.7 | 1.63 | 0 |
| Olivine (S) | 1.3 | 1.8 | 1.62 | 0.00001 |
| Olivine (M) | 2.6 | 5.0 | 1.62 | 0.00001 |
| Olivine (L) | 3.8 | 3.7 | 1.62 | 0.00001 |
| Olivine (XL) | 6.3 | 6.8 | 1.62 | 0.00001 |
| Volcanic ash (El Chichon) | 3.2 | 5.4 | 1.50–1.60 | 0.001 |
| Volcanic ash (Pinatubo) | 3.0 | 12.3 | 1.50–1.60 | 0.001–0.00001 |
| Volcanic ash (Lokon) | 7.1 | 2.6 | 1.50–1.60 | 0.001–0.00001 |
| Volcanic ash (Mnt. St. Helens) | 4.1 | 9.5 | 1.48–1.56 | 0.0018 |
| Volcanic ash (Redoubt A) | 4.1 | 9.7 | 1.48–1.56 | 0.0018 |
| Volcanic ash (Redoubt B) | 6.4 | 7.6 | 1.48–1.56 | 0.0018 |
| Volcanic ash (Spurr Ashton) | 2.7 | 4.9 | 1.48–1.56 | 0.0018–0.02 |
| Volcanic ash (Spurr Gunsight) | 3.5 | 8.2 | 1.48–1.56 | 0.0018–0.02 |
| Volcanic ash (Spurr Ahchorage) | 4.8 | 8.8 | 1.48–1.56 | 0.0018–0.02 |
| Volcanic ash (Spurr Stop 33) | 14.4 | 6.6 | 1.48–1.56 | 0.0018–0.02 |

Note. r_{eff} is the effective radius; v_{eff} is the variance; Re (m) and Im (m) are the real part and the imaginary part of the estimated refractive index, respectively.
^aThese samples have been investigated in Merikallio et al. (2011) for studying spheroid applicability.

Similar results were also obtained at 441.6 nm (data not shown). It can be seen that red clays' P_{22}/P_{11} and P_{44}/P_{11} demonstrated a scattering-angle dependence that was quite different from those of feldspar. Jin et al. (2016) employed the Koch-fractal model, which is really an irregular particle with complex small structures on surface, and successfully reproduce all six scattering matrix elements concurrently, although the refractive index $1.80 + i0.0005$ was much larger than the red clay's suggested values. A clear explanation about the features of P_{44}/P_{11} is still lacking.

Figure 11 shows the simulated results of the quartz sample and the corresponding measurements at a wavelength of 632.8 nm, in which quartz shows an effective radius of 2.3 μm and an effective variance of 2.3. The refractive index was estimated to be 1.54. Note that the refractive index used for modeling was $1.55 + i0.001$, which was slightly different from the measurement. As can be seen from the figure, the spheroidal model again demonstrates its incapability for use in modeling the scattering matrix based on an equi-probable distribution. However, superspheroids with a roundness parameter of 2.6 demonstrated fairly good agreement with the measurements. The group of superspheroids with a roundness parameter of 3.0 also performed reasonably well for all of the elements. A comparison at a wavelength of 441.6 nm was also conducted, but the results are not shown (the wavelength dependence will be studied in section 3.3).

3.3.2. Volcanic Ash

Volcanic ash is an important type of atmospheric aerosol, which can remain for a long time after being emitted into the stratosphere; thus, this ash has a great impact on the global climate. Comparisons between measurements and simulations were conducted for all 10 volcanic ash samples collected from different regions.

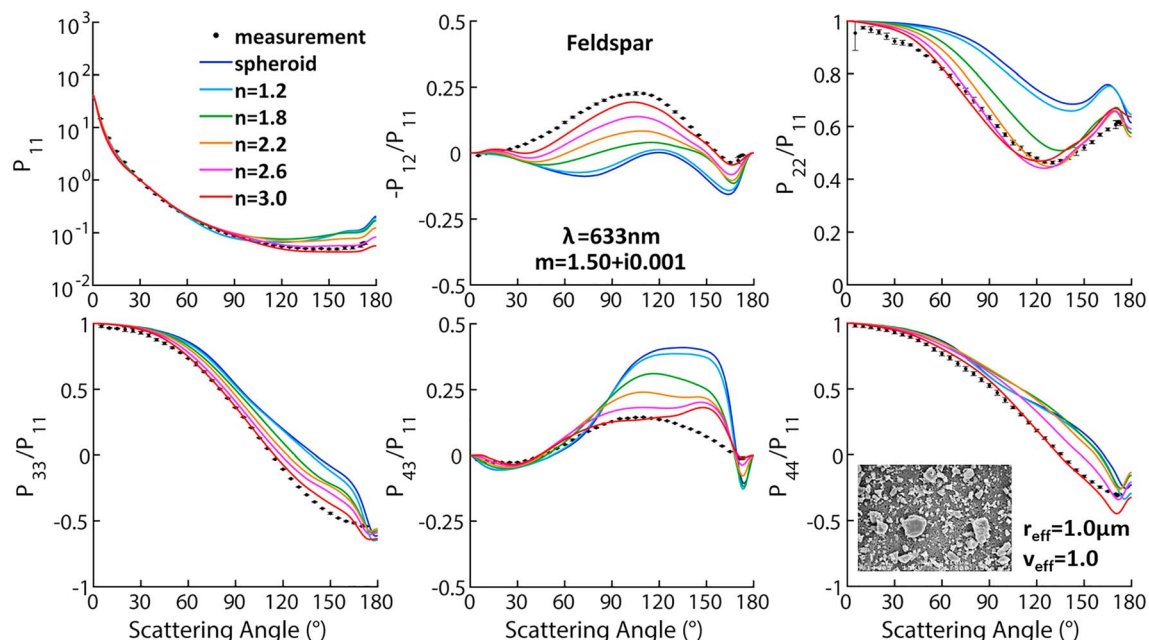


Figure 9. Comparison of scattering matrix elements between measurements and simulations with spheroids and superspheroids for feldspar at the 632.8-nm wavelength. The refractive index used for simulations was $1.50 + i0.001$, and an equi-probable aspect ratio distribution was used.

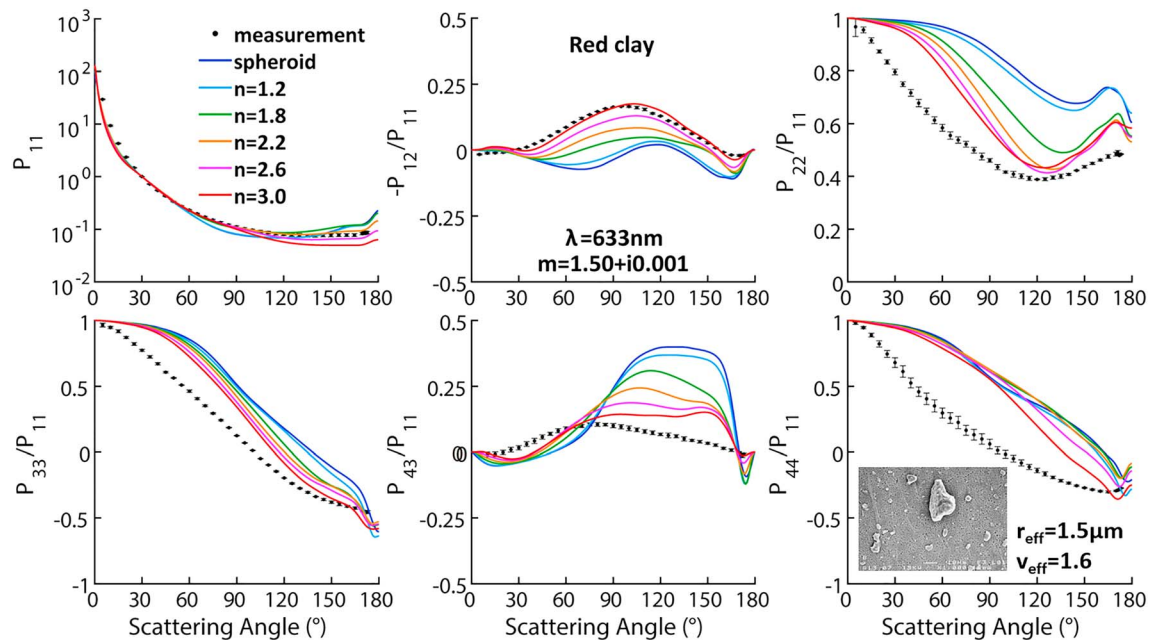


Figure 10. Similar to Figure 9, but the red clay sample is shown. The refractive index that was chosen for simulations was $1.50 + i0.001$.

Volcanic ash sample from the Pinatubo volcano in the Philippines had an effective radius of $3.0 \mu\text{m}$ and an effective variance of 12.3. The refractive index was estimated to be $1.50 - 1.60 + i0.00001 - 0.001$. The refractive index for the simulations was chosen to be $1.60 + i0.001$. Figure 12 shows the results of simulations and measurements at a wavelength of 632.8 nm . Not surprisingly, simulations with spheroids could not reproduce the scattering matrix elements especially for $-P_{12}/P_{11}$, P_{22}/P_{11} , and P_{43}/P_{11} . However, the use of superspheroids with roundness parameter of 2.6 and 3.0 successfully mimicked the measurements. It is noteworthy that $n = 2.6$ or $n = 3.0$ was also a good choice for a shape parameter for simulations at a wavelength of 441.6 nm (data not shown).

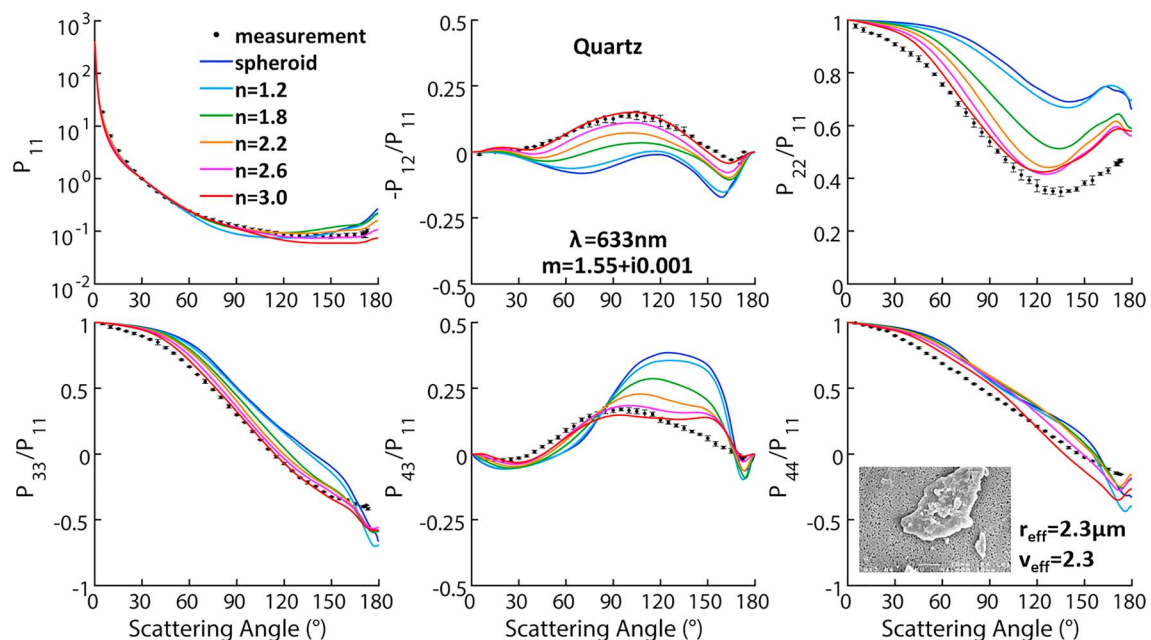


Figure 11. Similar to Figure 9, but the quartz sample is shown. The refractive index used for simulations was $1.55 + i0.001$.

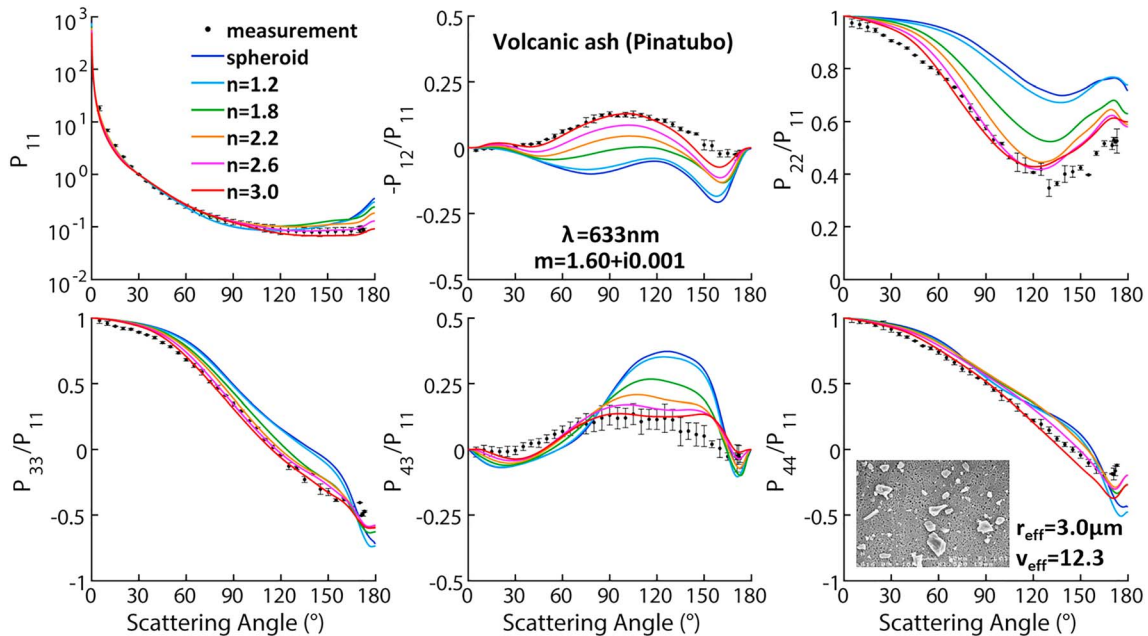


Figure 12. Similar to Figure 10 but for the Pinatubo sample is shown. The refractive index used for simulations was $1.60 + i0.001$.

Figure 13 shows the comparisons between measurements and simulations for another five volcanic ash samples from Mount St. Helens, Redoubt, and Mount Spurr volcanoes. The samples from Mount St. Helens were collected after a large eruption on 18 May 1980, and the Redoubt A samples are from the 1989 to 1990 eruptions. Both the Spurr Ashton and Spurr Anchorage samples were from the 18 August 1992 eruption, while the Spurr Stop 33 samples were from the 17 September 1992 eruption. The refractive index was chosen to be $1.60 + i0.001$ for all the five samples. Simulations with a roundness parameter of 2.6 or 3.0 were quite close to the measured $-P_{12}/P_{11}$ for all the five samples and the simulated values of P_{22}/P_{11} with roundness parameter of 3.0 slightly overestimated the measurements, while those of P_{11} underestimated the measurements especially at backscattering angles. An interesting finding observed in the figure is that the simulations of all the five samples demonstrate high similarity even though the effective radii and variances of the samples were quite different. Comparisons have also been conducted for another four volcanic ash samples: (1) El Chichon, (2) Lokon, (3) Redoubt B, and (4) Spurr Gunsight. However, the results are not shown here because they were similar to those presented in Figure 13.

3.3.3. Other Samples

Figure 14 shows the simulated and measured P_{11} , $-P_{12}/P_{11}$, and P_{22}/P_{11} at 632.8 nm for three forsterite samples that have different size distributions. The refractive index was chosen to be $1.60 + i0.001$ for all of the samples. The superspheroidal model worked best for the small forsterite sample with a roundness parameter of 3.0. The measured P_{11} and $-P_{12}/P_{11}$ of initial forsterite sample could also be reproduced. As is shown, the results of superspheroids slightly underestimate the phase function and overestimate the P_{22}/P_{11} of washed forsterite sample, which has the largest effective radius and variance. A larger refractive index (with a real part of 1.70) was also applied to the simulations of the washed forsterite sample. In this case, the phase function could be reproduced with a roundness parameter of 2.6 (not shown). However, mimicking the P_{22}/P_{11} is still challenging. Nevertheless, superspheroids appear to be much better than spheroids.

Results of four olivine samples with different size distribution are shown in Figure 15. The refractive index remained at $1.65 + i0.001$ for all the samples. Similar to the cases of forsterite, the superspheroidal model worked better for the samples with small effective radius. An appropriate roundness parameter for simulations was selected to be 2.6 for the olivine (S) and olivine (M) samples. As shown in the figure, when the effective radius becomes larger, the simulated P_{11} and P_{22}/P_{11} appear to become worse, underestimating the

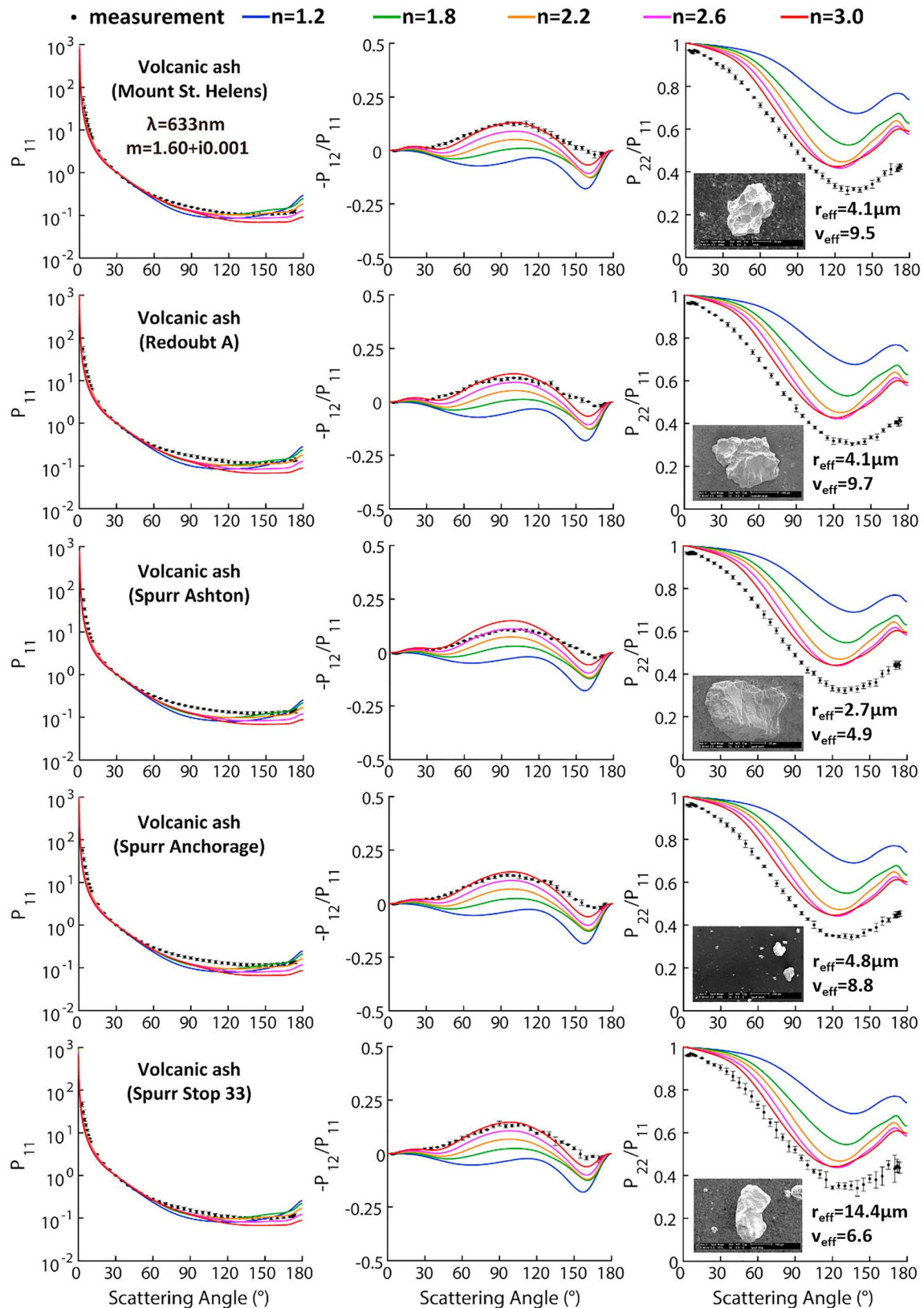


Figure 13. Three key scattering matrix elements (P_{11} , $-P_{12}/P_{11}$, and P_{22}/P_{11}) of simulations and measurements at 632.8-nm wavelength for five volcanic ash samples. The refractive index was selected to be $1.60 + i0.001$ for all the samples.

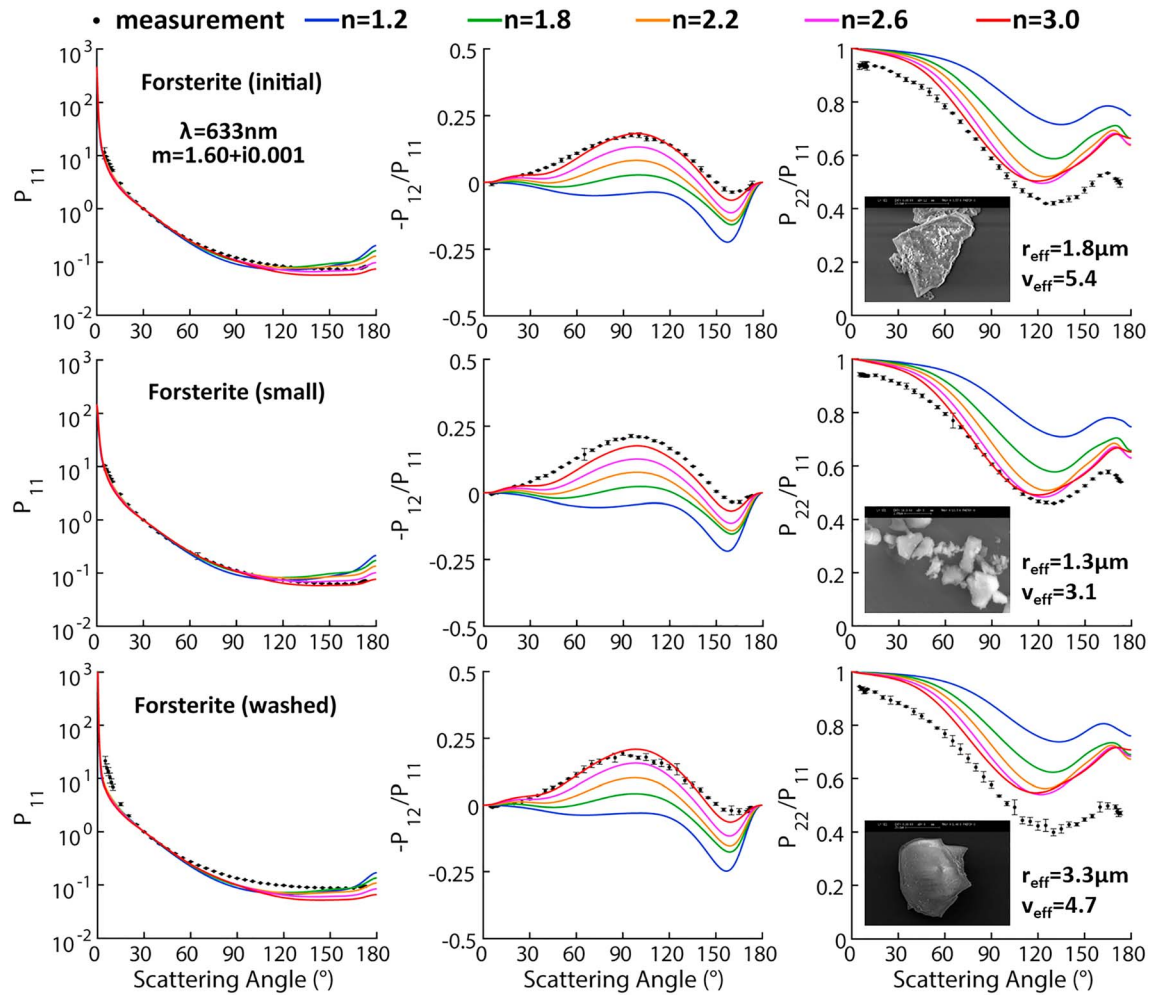


Figure 14. Three scattering matrix elements (P_{11} , $-P_{12}/P_{11}$, and P_{22}/P_{11}) of simulations and measurements at 632.8-nm wavelength for three forsterite samples with different size distributions.

values of P_{11} and overestimating the P_{22}/P_{11} . Although the simulated curve of P_{22}/P_{11} approaches the measured one, as the roundness parameter increases from 1.0 to 3.0, relatively large differences can still be observed for all the four samples.

Figure 16 shows the results for another five samples: (1) Allende, (2) green clay, (3) loess, (4) Martian analog (palagonite), and (5) Sahara sand. The effective radius and effective variance of each sample and the refractive index used for simulations for each sample are shown in the figure. Agreement with the measurements could be obtained for P_{11} and $-P_{12}/P_{11}$ of the Allende sample if we used superspheroids with an appropriate roundness parameter of 2.6. For loess and Martian analog samples, superspheroids with a roundness parameter of 2.6 could concurrently mimic the measured P_{11} , $-P_{12}/P_{11}$, and P_{22}/P_{11} . However, as seen in the figure, superspheroids fail to reproduce the elements of the Sahara sand sample, which had a large effective radius ($8.2 \mu\text{m}$) and high uncertainty in the measurements, especially for $-P_{12}/P_{11}$ and P_{22}/P_{11} . It is understandable that morphological details become relatively more important as the size increases.

3.4. Wavelength Dependence

In this section, we investigated the wavelength dependence of scattering matrix elements of dust aerosols. An appropriate roundness parameter for each sample is selected for simulations at both 441.6- and 632.8-nm wavelengths. The refractive index is assumed to be unchanged at different wavelengths. An

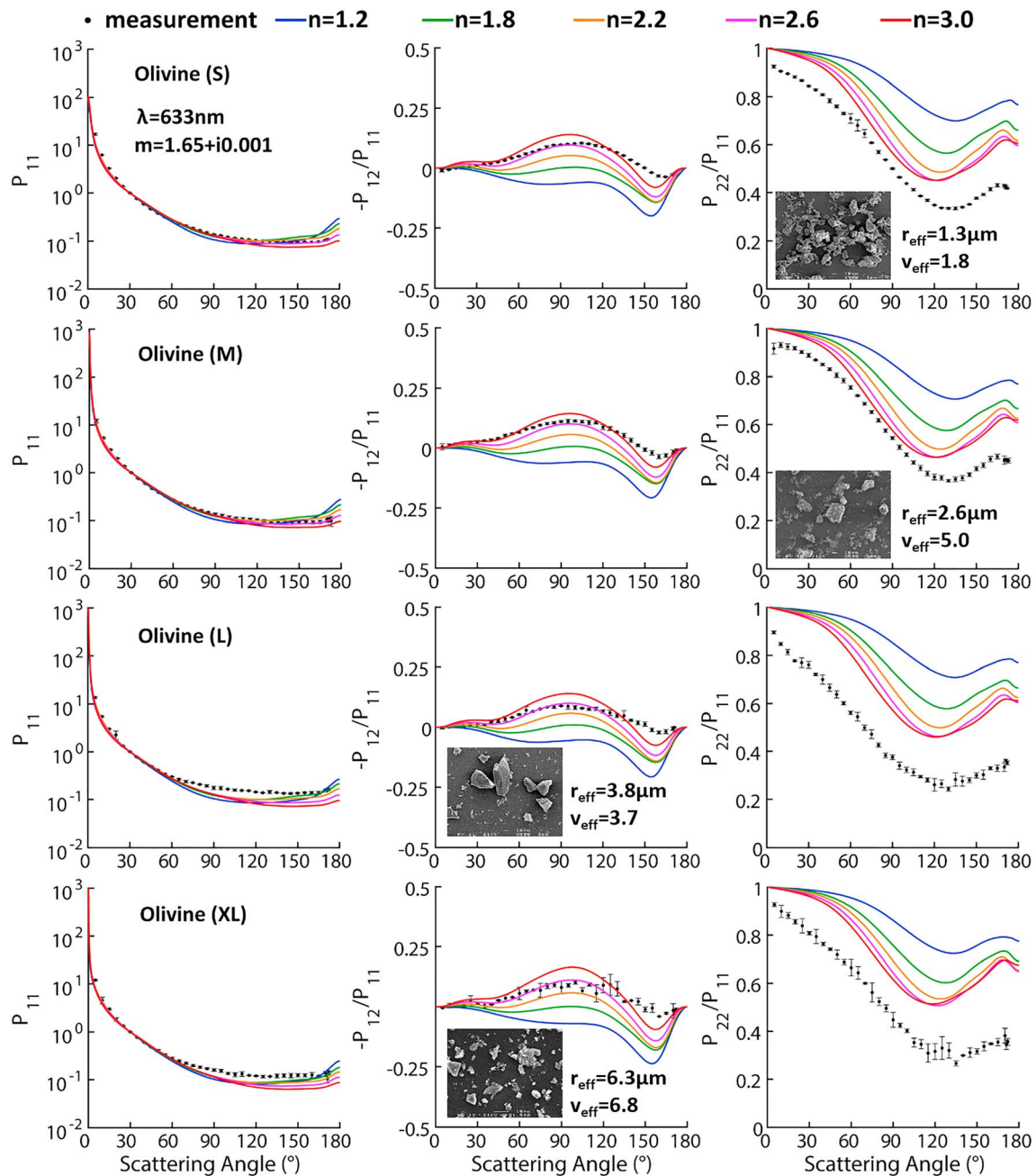


Figure 15. Similar to Figure 14, but results for four olivine samples are shown.

equi-probable aspect ratio is still applied to superspheroids, while a power law aspect ratio distribution is applied to spheroids. Specifically, the equation shown below was used to represent the shape distribution of spheroids (Kahnert et al., 2002; Merikallio et al., 2011),

$$p(\zeta) = \frac{|\zeta|^s}{\int_{\zeta_{\min}}^{\zeta_{\max}} |\zeta|^s d\zeta}; s \geq 0, \quad (8)$$

where ζ is a shape parameter, and is defined as

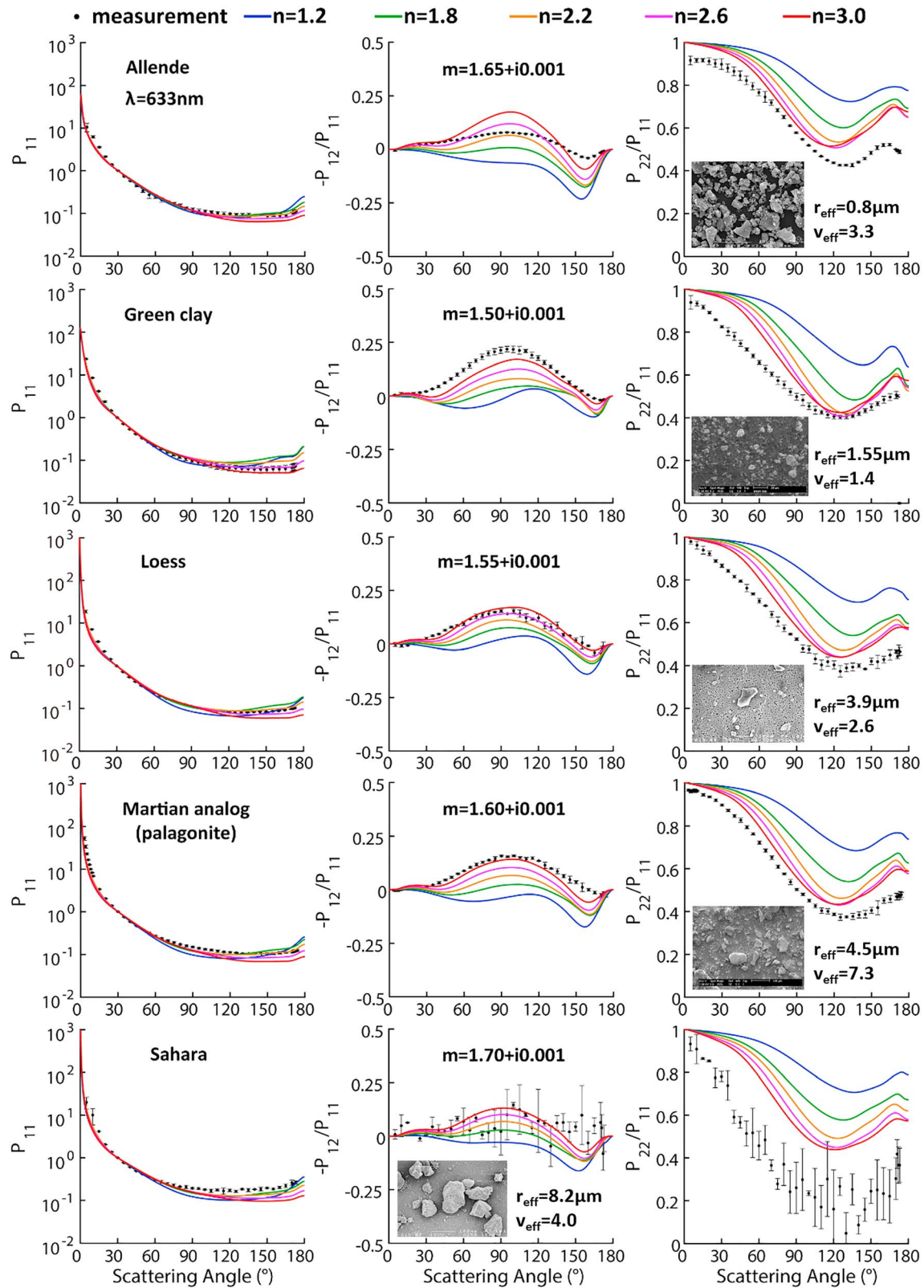


Figure 16. Similar to Figure 14, but the Allende, green clay, loess, Martian analog (palagonite), and Sahara sand samples are shown.

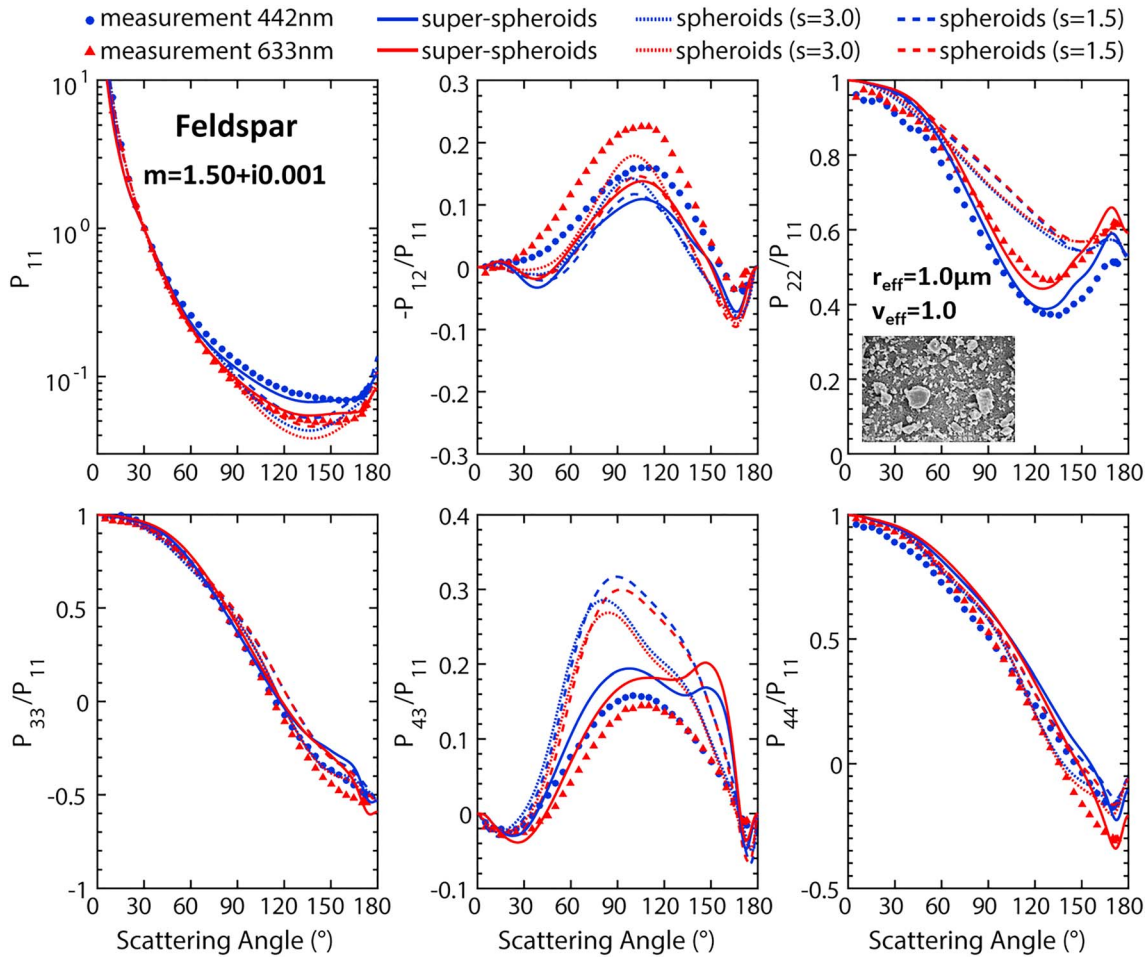


Figure 17. Comparison of scattering matrix elements between measurements and simulations with spheroids and superspheroids for feldspar at both 441.6- and 632.8-nm wavelengths. The roundness parameter of superspheroids is 2.6. The dotted and dashed curves represent the results of spheroids with a power law aspect ratio distribution (ξ^s), $s = 3.0$, and $s = 1.5$, respectively.

$$\xi = \begin{cases} c/a - 1; & (\text{oblate spheroid}) \\ 1 - a/c; & (\text{prolate spheroid}) \end{cases} \quad (9)$$

Note that extreme aspect ratios are now employed for spheroids, and thus, there are in total 18 different aspect ratios (namely, 0.3–1.0 in increments of 0.1 and 1.2–3.0 in increments of 0.2). Obviously, $\xi = 0$ and $p(\xi) = 0$ for a sphere. The results of spheroids with an equi-probable shape distribution are not presented in this section because they are incapable in reproducing the measured scattering matrix elements of dust aerosols even though the extreme aspect ratios are employed.

Figure 17 shows the plot of the six nonzero scattering matrix elements of simulations and measurements at both 441.6- and 632.8-nm wavelengths for the feldspar sample. The refractive index was chosen to be $1.50 + i0.001$, and 2.6 was used as the superspheroids' roundness parameter. As demonstrated in Figure 17, the measured scattering matrix shows distinguishable wavelength dependence. Simulations with spheroids with a power law shape distribution ($s = 3.0$ for dotted curves and $s = 1.5$ for dashed curves) fail to reproduce such pronounced spectral dependence especially for P_{22}/P_{11} , which is nearly identical at both wavelengths. Spheroids with $s = 1.5$ could reproduce the measured phase function at 632.8 nm better than those with $s = 3.0$, but other simulated elements show larger difference with the measurements. Superspheroids perform better than spheroids in matching the measured phase function and P_{22}/P_{11} at both wavelengths. Both spheroids and superspheroids show relatively large differences for reproducing the spectral dependence found in $-P_{12}/P_{11}$. It should be noted that the comparison with $-P_{12}/P_{11}$ could be improved by changing

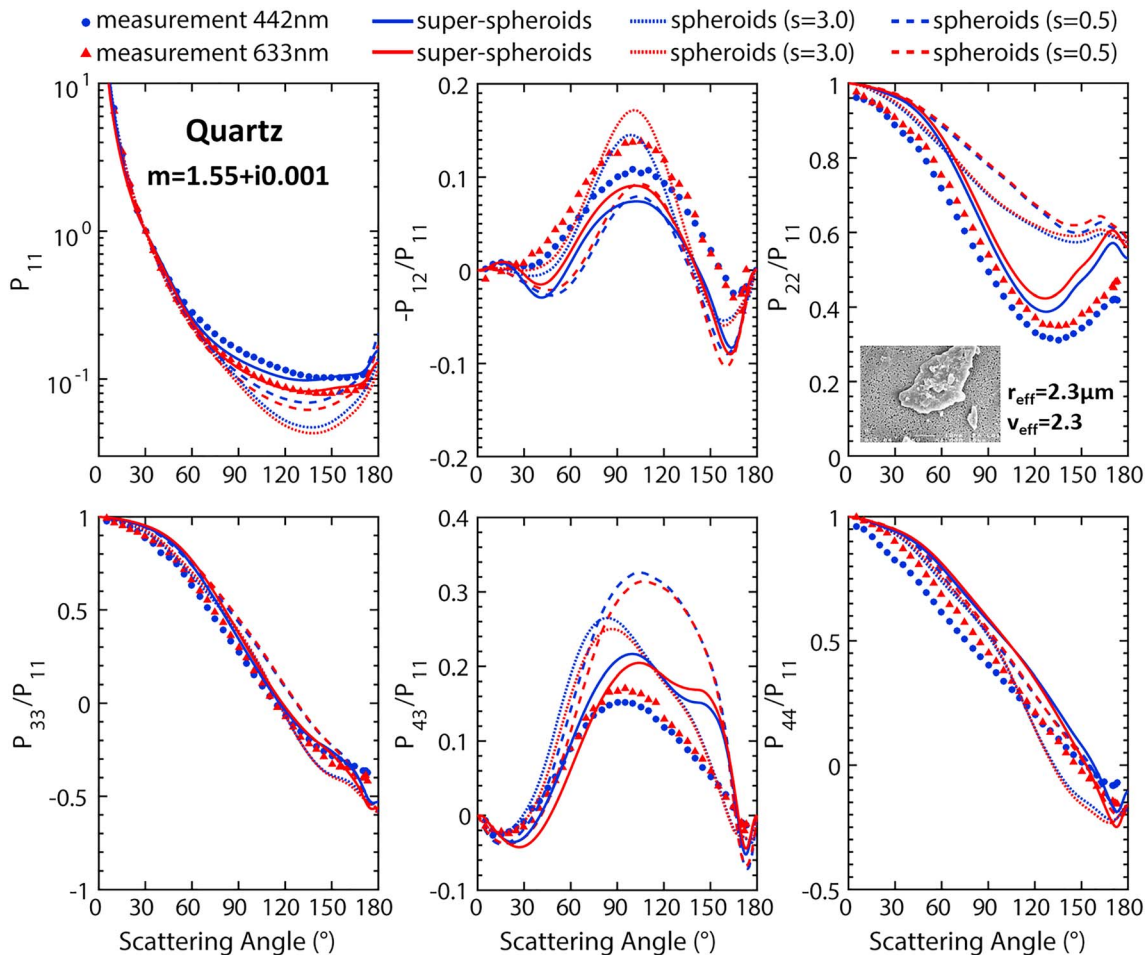


Figure 18. Similar to Figure 17, but for the quartz sample. The roundness parameter of superspheroids is 2.4. The dotted curves and dashed curves represent the results of spheroids with a power law aspect ratio distribution (ξ^s), $s = 3.0$, and $s = 0.5$, respectively.

the roundness parameter, but the other elements would become worse. Such inconsistency still exists in the superspheroidal model, but superspheroids have an overall better performance than spheroids for all the elements including P_{43}/P_{11} .

Figure 18 is similar to Figure 17 but represents the quartz sample. The superspheroids' roundness parameter was chosen to be 2.4, which is the optimal shape parameter for mimicking the phase function at 632.8-nm wavelength. In the case of $s = 3.0$, the simulated $-P_{12}/P_{11}$ of spheroids shows pronounced spectral dependence. With $s = 0.5$, the simulated phase function of the spheroids approached the measurements, but the other simulated elements became worse. Simulations with superspheroids performed better than other ones, although inconsistencies still exist for the best matching different elements. It can be seen that simulations with spheroids showed little wavelength dependence on P_{22}/P_{11} at near-backscattering angles. However, such characteristics are usually found in simulations with superspheroids although the simulated results have relatively large difference from the measurements. Overall, the simulations with superspheroids for quartz sample were in line with the measurements. Exactly matching the ratio P_{22}/P_{11} is usually challenging in the cases of most samples. Note that we have not employed any tuning procedure in terms of shape distribution, except for a constrained roundness parameter.

The results of volcanic ash sample from Pinatubo are shown in Figure 19. The refractive index is $1.60 + i0.001$, and the roundness parameter of superspheroids is 2.6. As demonstrated in the figure, superspheroids are more applicable than spheroids for almost all the scattering matrix elements, especially for the phase function and P_{22}/P_{11} . Similar to the case of the quartz sample, the superspheroids were shown to perform much better than spheroids in mimicking the measured scattering matrix elements at both wavelengths.

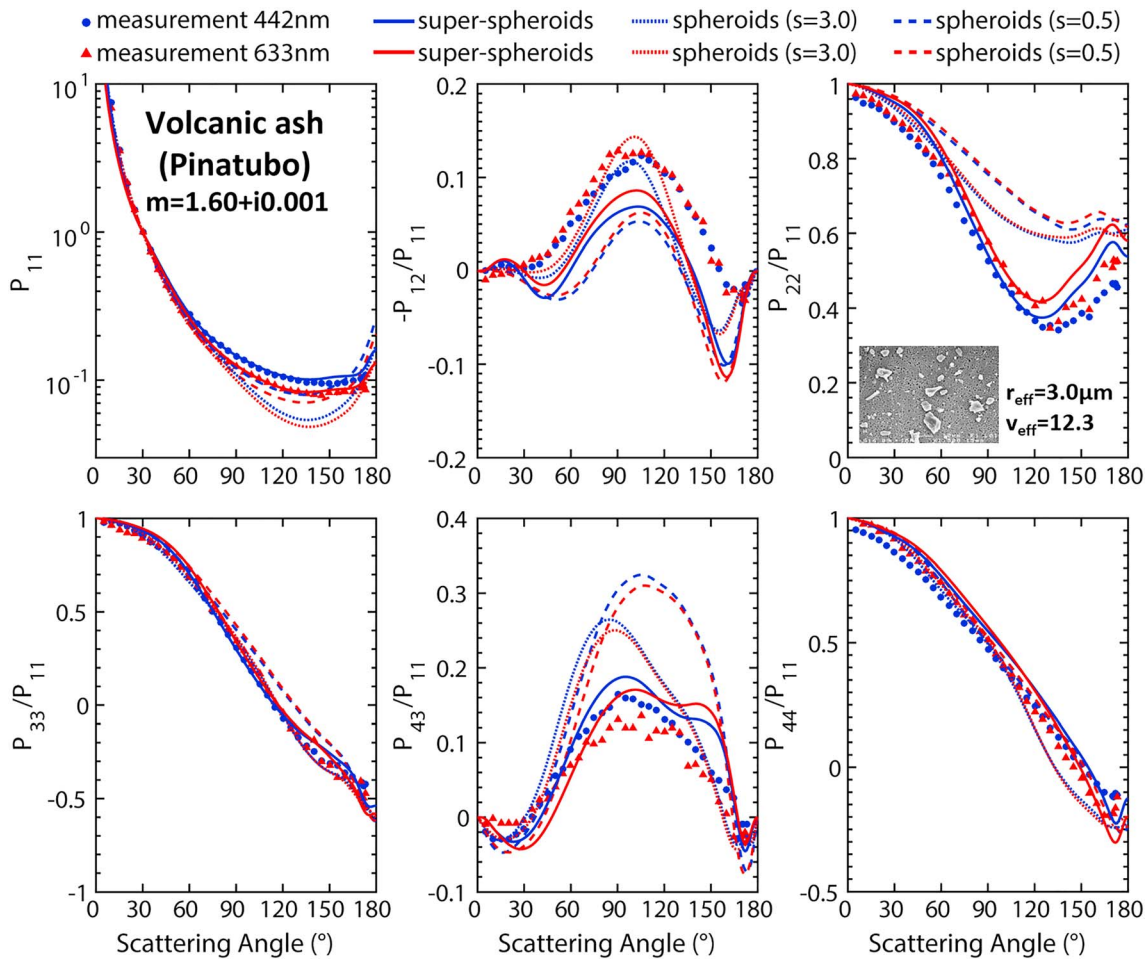


Figure 19. Similar to Figure 18, but the results of the volcanic ash sample from Pinatubo are shown. The roundness parameter of superspheroids is 2.6.

Figure 19 shows the results of the olivine sample. The optimal roundness parameter of superspheroids is 2.4, which works well for P_{11} at both wavelengths. However, large difference between simulations and measurements were found for $-P_{12}/P_{11}$. The simulated $-P_{12}/P_{11}$ would get close to the measured ones if a roundness parameter of 2.6 was applied. Thus, a compromise is usually inevitable in actual applications. But as illustrated from the figure, superspheroids with an equi-probable shape distribution still perform better than spheroids with a power law shape distribution, especially for P_{11} , P_{22}/P_{11} , and P_{43}/P_{11} .

From these comparisons shown in Figures 17–20, we learned that superspheroids are not perfect but significantly improve the overall performance in concurrently modeling all the scattering matrix elements at two wavelengths. This observed fact is similar to all of the other samples (not shown).

3.5. Modeling Uncertainties

Our present study demonstrated that the use of superspheroids that had an appropriate roundness parameter could be used to reproduce the measured P_{11} , $-P_{12}/P_{11}$, and P_{22}/P_{11} with good consistency for most of the samples even though an equi-probable aspect ratio distribution was applied. It should be noted that a number of factors may affect the accuracy of the simulated results in the modeling of scattering matrix of dust aerosols. First, the refractive index of dust aerosols may be size dependent because chemical compositions change with particle size (Otto et al., 2008). The way in which the size-dependent refractive index impacted the scattering was not systematically investigated in the current study. Also, the imaginary part of refractive index could be spectrally dependent. However, from the sensitivity studies related to the refractive index shown in the study by Zubko et al. (2013), the imaginary part of the refractive index had little impact on the scattering matrices as it increased from 0 to 0.01. Second, measuring size distribution is not

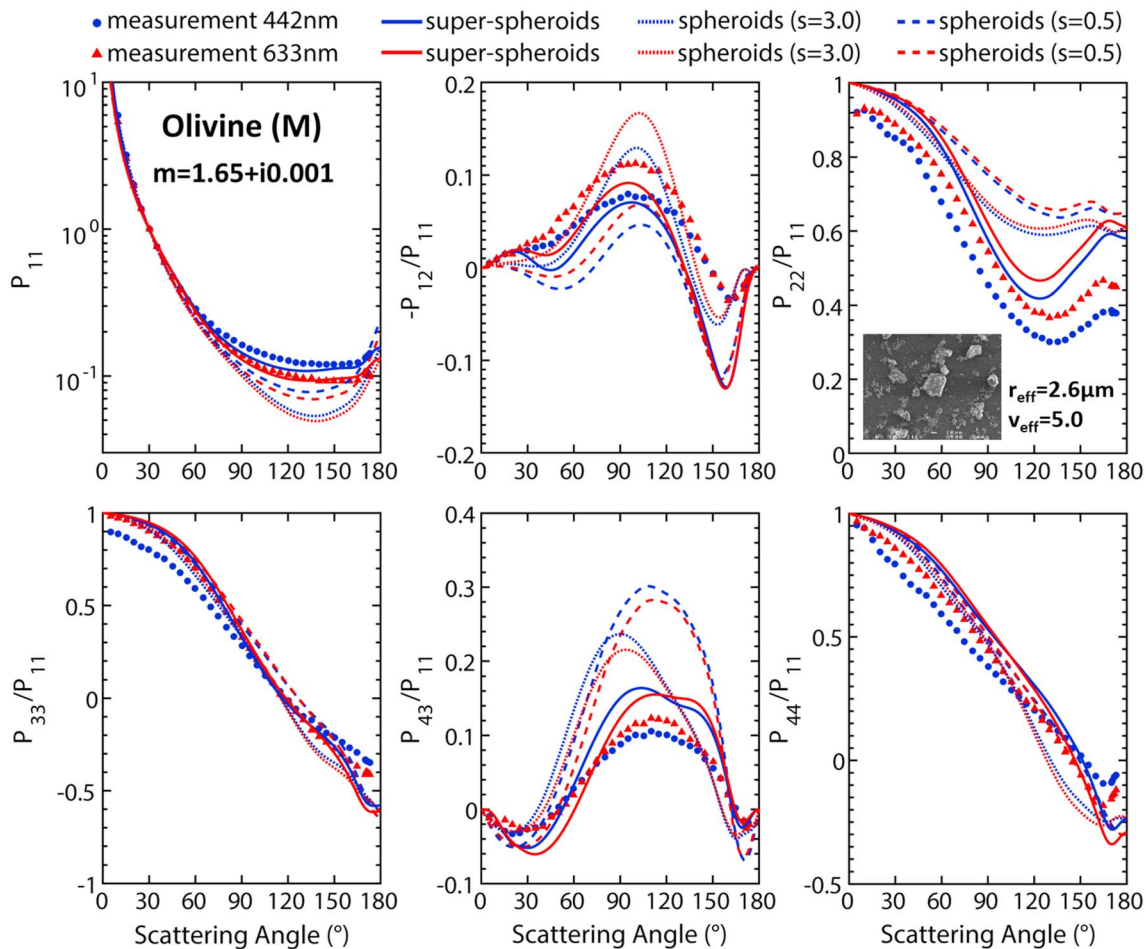


Figure 20. Similar to Figure 18, but the results of the olivine (M) sample from are shown. The roundness parameter of superspheroids is 2.4.

a straightforward task and the size distribution of each sample obtained in the laboratory may have uncertainties. For example, the use of the Fraunhofer diffraction to retrieve the particle sizes has the restriction that the particles under study must be sufficiently large compared with the wavelength of the incident light. However, this size distribution uncertainty is assumed to be a relatively minor factor in constraining suitable roundness parameter range for reproducing the measured scattering characteristics. Third, the shapes of dust particle were shown to be size dependent. For simplicity, such complicated shape variations in particle sizes are rarely considered. Instead, an overall shape distribution is often applied to optical modeling; namely, the shape distribution is the same for all the size bins. In addition, small-scale surface roughness was another important factor that affected the scattering of dust aerosols. Surface roughness tends to smoothen the phase function, promote positive linear polarization at side-scattering angles, and strengthen depolarization (Nousiainen, 2009). In the current study, theoretical simulations normally approached the P_{22}/P_{11} element from above by increasing the roundness parameter. The way in which small-scale roughness of superspheroidal model impacts P_{22}/P_{11} modeling would be necessary because simulations seem to be systematically larger than measurements for most samples. However, this study is out of the scope of the present study. To summarize, it is important to mention that one should consider uncertainties in all aerosol parameters including shapes, size distribution, and refractive index and its spectral dependence to really match measurements. Thus, discrepancies in the comparisons could not be definitely related to the shape model used, although it is difficult to prove. Moreover, measurements might have some uncertainties. For example, the magnitudes of scattering signals in small angles are too high to measure. Note that P_{22}/P_{11} from measurements could has offset and not 1 even at near forward scattering angles (e.g., Figure 20), indicating possible involved uncertainties.

Nevertheless, based on the present study, measurement uncertainties could be fairly minor in causing large model-measurement discrepancies.

4. Summary and Discussion

We introduced the superspheroidal model for computing the scattering matrix of dust aerosols. In addition to the aspect ratio, superspheroids have another shape parameter, namely, the roundness parameter, which permits more morphological variations and thus can mimic more dust particles' characteristics (such as concavity and sharp edge). Comparisons of scattering matrix elements between spheroids and superspheroids demonstrated that major characteristics of measured scattering matrix elements of dust aerosol samples (more or less) could be obtained in two ways. One involved the use of changing the aspect ratio to a value that departs the most from unity. The other way involved the use of large roundness parameters, which indicates that concave superspheroids could be practical in modeling the scattering matrix of dust aerosols. By comparing with measurements from the Amsterdam-Granada Light Scattering Database (Muñoz et al., 2000, 2004, 2012; Volten et al., 2000, 2006, 2007), our study shows that extreme aspect ratios (>2.0 or <0.5) for spheroids in reproducing the measurements are unnecessary for superspheroids, and an optimal range for superspheroids' roundness parameters in modeling the scattering matrix of dust aerosols was found to be [2.4, 3.0]. Further analysis showed that superspheroids with constrained roundness parameters appear to be much better than spheroids (a unity roundness parameter) even though extreme aspect ratios of spheroids are considered.

The superiorities of superspheroids over spheroids can be summarized as follows: (1) An equi-probable aspect ratio distribution can be used to obtain a favorable agreement between simulations and measurements. However, the aspect ratio distribution of spheroids has to be carefully tuned to reproduce the measured scattering matrix elements of dust sample; this tuning process could be dependent on the specific element of the scattering matrix. (2) Overall, superspheroids are much better than spheroids to simulate the wavelength dependence of scattering matrix. Spheroids suffer more from the performance inconsistency, particularly in modeling the phase function and polarization characteristics (e.g., $-P_{12}/P_{11}$ and P_{22}/P_{11}). (3) If a generic roundness parameter is chosen (e.g., $n = 2.6$), the superspheroidal model has identical freedom as the spheroidal model. Thus, the superspheroidal model retains the rule of simplicity. This might be a significant advantage for superspheroids for a general purpose modeling study. The impact of these superiorities in remote sensing applications and radiative forcing simulations remains to be explored.

Acknowledgments

This study was supported by the National Natural Science Foundation of China (41675025), the National Key Research and Development Program of China (2016YFC0200700), the Fundamental Research Funds for the Central Universities (2017QNA3017), and Zhejiang University K. P. Chao's High Technology Development Foundation. A portion of the computations was performed at the National Supercomputer Center in Guangzhou (NSCC-GZ) and the cluster at State Key Lab of CAD&CG at Zhejiang University. We appreciate three reviewers' constructive comments on improving the manuscript. The measured data of various aerosol samples in this study can be accessed from <https://www.iaa.csic.es/scattering/>. All simulated data displayed in figures are available on Github at https://github.com/bileihz/dust_modeling.

References

- Andreae, M. O. (1995). Chapter 10. Climatic effects of changing atmospheric aerosol levels. *World Survey of Climatology*, 16(6), 347–398.
- Arimoto, R. (2001). Eolian dust and climate: Relationships to sources, tropospheric chemistry, transport and deposition. *Earth-Science Reviews*, 54(1–3), 29–42.
- Barr, A. H. (1981). Superquadrics and angle preserving transformation. *IEEE Computer Graphics and Applications*, 1, 11–23.
- Bi, L., Lin, W., Liu, D., & Zhang, K. (2018). Assessing the depolarization capabilities of non-spherical particles in a super-ellipsoidal shape space. *Optics Express*, 26(2), 1726–1742.
- Bi, L., Lin, W., Wang, Z., Tang, X., Zhang, X., & Yi, B. (2018). Optical modeling of sea salt aerosols: The effects of nonsphericity and inhomogeneity. *Journal of Geophysical Research: Atmospheres*, 123, 543–558. <https://doi.org/10.1002/2017JD027869>
- Bi, L., & Yang, P. (2014). Accurate simulation of the optical properties of atmospheric ice crystals with the invariant imbedding T-matrix method. *Journal of Quantitative Spectroscopy and Radiative Transfer*, 138, 17–35.
- Bi, L., Yang, P., Kattawar, G. W., & Kahn, R. (2009). Single-scattering properties of triaxial ellipsoidal particles for a size parameter range from the Rayleigh to geometric-optics regimes. *Applied Optics*, 48(1), 114–126.
- Bi, L., Yang, P., Kattawar, G. W., & Kahn, R. (2010). Modeling optical properties of mineral aerosol particles by using nonsymmetric hexahedra. *Applied Optics*, 49(3), 334–342.
- Bi, L., Yang, P., Kattawar, G. W., & Mishchenko, M. I. (2013a). Efficient implementation of the invariant imbedding T-matrix method and the separation of variables method applied to large non-spherical inhomogeneous particles. *Journal of Quantitative Spectroscopy and Radiative Transfer*, 116, 169–183.
- Bi, L., Yang, P., Kattawar, G. W., & Mishchenko, M. I. (2013b). A numerical combination of extended boundary condition method and invariant imbedding method to light scattering by large spheroids and cylinders. *Journal of Quantitative Spectroscopy and Radiative Transfer*, 123, 17–22.
- Bohren, C. F., & Huffman, D. R. (1983). *Absorption and scattering of light by small particles*. New York: John Wiley.
- Chiapello, I., Bergametti, G., Chatenet, B., Dulac, F., Jankowiak, I., Liousse, C., & Soares, E. S. (1999). Contribution of the different aerosol species to the aerosol mass load and optical depth over the northeastern tropical Atlantic. *Journal of Geophysical Research*, 104, 4025–4035. <https://doi.org/10.1029/1998JD200044>
- Chou, C., Formenti, P., Maille, M., Ausset, P., Helas, G., Harrison, M., & Osborne, S. (2008). Size distribution, shape, and composition of mineral dust aerosols collected during the African Monsoon Multidisciplinary Analysis Special Observation Period 0: Dust and Biomass-Burning Experiment field campaign in Niger, January 2006. *Journal of Geophysical Research*, 113, D00C10. <https://doi.org/10.1029/2008JD009897>

- D'Almeida, G. A., Koepke, P., & Shettle, E. P. (1991). Atmospheric aerosols: Global climatology and radiative characteristics. *Journal of Medical Microbiology*, *54*(1), 55–61.
- Dubovik, O., Herman, M., Holdak, A., Lapyonok, T., Tanré, D., Deuzé, L., et al. (2011). Statistically optimized inversion algorithm for enhanced retrieval of aerosol properties from spectral multi-angle polarimetric satellite observations. *Atmospheric Measurement Techniques*, *4*, 975–1018.
- Dubovik, O., Holben, B. N., Lapyonok, T., Sinyuk, A., Mishchenko, M. I., Yang, P., & Slutsker, I. (2002). Non-spherical aerosol retrieval method employing light scattering by spheroids. *Geophysical Research Letters*, *29*(10), 1415. <https://doi.org/10.1029/2001GL014506>
- Dubovik, O., Sinyuk, A., Lapyonok, T., Holben, B. N., Mishchenko, M. I., Yang, P., et al. (2006). Application of spheroid models to account for aerosol particle nonsphericity in remote sensing of desert dust. *Journal of Geophysical Research*, *111*, D11208. <https://doi.org/10.1029/2005JD006619>
- Feng, Q., Yang, P., Kattawar, G. W., Hsu, C. N., Tsay, S. C., & Laszlo, I. (2009). Effects of particle nonsphericity and radiation polarization on retrieving dust properties from MODIS observations. *Journal of Aerosol Science*, *40*(9), 776–789.
- Gao, Y., & Anderson, J. R. (2001). Characteristics of Chinese aerosols determined by individual particle analysis. *Journal of Geophysical Research*, *106*, 18,037–18,045.
- Ginoux, P., Chin, M., Tegen, I., Prospero, J. M., Holben, B., Dubovik, O., & Lin, S. J. (2001). Sources and distributions of dust aerosols simulated with the GOCART model. *Journal of Geophysical Research*, *106*(D17), 20,255–20,273. <https://doi.org/10.1029/2000JD000053>
- Ginoux, P., Prospero, J. M., Torres, O., & Chin, M. (2004). Long-term simulation of dust distribution with the GOCART model: Correlation with the North Atlantic Oscillation. *Environmental Modeling and Software*, *19*, 113–128.
- Govaerts, Y. M., Wagner, S., Lattanzio, A., & Watts, P. (2010). Joint retrieval of surface reflectance and aerosol optical depth from MSG/SEVIRI observations with an optimal estimation approach: 1. Theory. *Journal of Geophysical Research*, *111*, D02203. <https://doi.org/10.1029/2009JD011779>
- Haywood, J., & Boucher, O. (2000). Estimates of the direct and indirect radiative forcing due to tropospheric aerosols: A review. *Reviews of Geophysics*, *38*(4), 513–543. <https://doi.org/10.1029/1999RG000078>
- Haywood, J., Francis, P., Osborne, S., Glew, M., Loeb, N., Highwood, E., et al. (2003). Radiative properties and direct radiative effect of Saharan dust measured by the C-130 aircraft during SHADE. 1. Solar spectrum. *Journal of Geophysical Research*, *108*(D18), 8577. <https://doi.org/10.1029/2002JD002687>
- Haywood, J. M., Francis, P. N., Glew, M. D., & Taylor, J. P. (2001). Optical properties and direct radiative effect of Saharan dust: A case study of two Saharan dust outbreaks using aircraft data. *Journal of Geophysical Research*, *106*(D16), 18,417–18,430. <https://doi.org/10.1029/2000JD900319>
- Hess, M., Koepke, P., & Schult, I. (1998). Optical Properties of Aerosols and Clouds: The software package OPAC. *Bulletin of the American Meteorological Society*, *79*(5), 831–844.
- Huang, X., Yang, P., Kattawar, G., & Liou, K. N. (2015). Effect of mineral dust aerosol aspect ratio on polarized reflectance. *Journal of Quantitative Spectroscopy and Radiative Transfer*, *151*, 97–109.
- Jin, C., Liu, C., Yin, Y., Bi, L., & Nousiainen, T. (2016). Modeling the scattering matrix of red clays. *Optics Letters*, *41*(21), 4879–4882.
- Kahnert, F. M., Stamnes, J. J., & Stamnes, K. (2002). Using simple particle shapes to model the Stokes scattering matrix of ensembles of wavelength-sized particles with complex shapes: Possibilities and limitations. *Journal of Quantitative Spectroscopy and Radiative Transfer*, *74*, 167–182.
- Kahnert, M., & Nousiainen, T. (2006). Uncertainties in measured and modelled asymmetry parameters of mineral dust aerosols. *Journal of Quantitative Spectroscopy and Radiative Transfer*, *100*, 173–178.
- Kahnert, M., Nousiainen, T., & Lindqvist, H. (2014). Review: Model particles in atmospheric optics. *Journal of Quantitative Spectroscopy and Radiative Transfer*, *146*, 41–58.
- Kahnert, M., Nousiainen, T., & Räisänen, P. (2007). Mie simulations as an error source in mineral aerosol radiative forcing calculations. *Quarterly Journal of the Royal Meteorological Society*, *133*, 299–307.
- Kahnert, M., Nousiainen, T., & Veihelmann, B. (2005). Spherical and spheroidal model particles as an error source in aerosol climate forcing and radiance computations: A case study for feldspar aerosols. *Journal of Geophysical Research*, *110*, D18513. <https://doi.org/10.1029/2004JD005558>
- Kalashnikova, O. V., & Sokolik, I. N. (2004). Modeling the radiative properties of non-spherical soil-derived mineral aerosols. *Journal of Quantitative Spectroscopy and Radiative Transfer*, *87*(2), 137–166.
- Kandler, K., Lieke, K., Benker, N., Emmel, C., Küpper, M., Müller-Ebert, D., et al. (2011). Electron microscopy of particles collected at Praia, Cape Verde, during the Saharan Mineral Dust Experiment: Particle chemistry, shape, mixing state and complex refractive index. *Tellus Series B: Chemical and Physical Meteorology*, *63*, 475–496.
- Kaufman, Y. J., Tanré, D., & Boucher, O. (2002). A satellite view of aerosols in the climate system. *Nature*, *419*, 215–222.
- Kaufman, Y. J., Tanré, D., Dubovik, O., Karnieli, A., & Remer, L. A. (2001). Absorption of sunlight by dust as inferred from satellite and ground-based remote sensing. *Geophysical Research Letters*, *28*(8), 1479–1482. <https://doi.org/10.1029/2000GL012647>
- Konare, A., Zakey, A. S., Solmon, F., Giorgi, F., Rauscher, S., Ibrah, S., & Bi, X. (2008). A regional climate modeling study of the effect of desert dust on the west African monsoon. *Journal of Geophysical Research*, *113*, D12206. <https://doi.org/10.1029/2007JD009322>
- Levy, R. C., Remer, L. A., & Dubovik, O. (2007). Global aerosol optical models and application to Moderate Resolution Imaging Spectroradiometer aerosol retrieval over land. *Journal of Geophysical Research*, *112*, D13210. <https://doi.org/10.1029/2006JD007815>
- Levy, R. C., Remer, L. A., Mattoo, S., Vermote, E. F., & Kaufman, Y. J. (2007). Second-generation operational algorithm: Retrieval of aerosol properties over land from inversion of Moderate Resolution Imaging Spectroradiometer spectral reflectance. *Journal of Geophysical Research*, *112*, D13211. <https://doi.org/10.1029/2006JD007811>
- Li, Z., Goloub, P., Devaux, C., Gu, X., Deuzé, J.-L., Qiao, Y., & Zhao, F. (2006). Retrieval of aerosol optical and physical properties from ground-based spectral, multi-angular, and polarized Sun-photometer measurements. *Remote Sensing of Environment*, *101*, 519–533.
- Liu, C., Panetta, R. L., Yang, P., Macke, A., & Baran, A. J. (2013). Modeling the scattering properties of mineral aerosols using concave fractal polyhedra. *Applied Optics*, *52*, 640–652.
- Liu, J., Zhang, Y., Zhang, Q., & Wang, J. (2018). Scattering matrix for typical urban anthropogenic origin cement dust and discrimination of representative atmospheric particulates. *Journal of Geophysical Research: Atmospheres*, *123*, 3159–3174. <https://doi.org/10.1002/2018JD028288>
- Merikallio, S., Lindqvist, H., Nousiainen, T., & Kahnert, M. (2011). Modelling light scattering by mineral dust using spheroids: Assessment of applicability. *Atmospheric Chemistry and Physics*, *11*, 5347–5363.

- Mishchenko, M. I., Geogdzhayev, I. V., Liu, L., Ogren, J. A., Lacis, A. A., Rossow, W. B., et al. (2003). Aerosol retrievals from AVHRR radiances: Effects of particle nonsphericity and absorption and an updated long-term global climatology of aerosol properties. *Journal of Quantitative Spectroscopy and Radiative Transfer*, *79*(80), 953–972.
- Mishchenko, M. I., Lacis, A. A., Carlson, B. E., & Travis, L. D. (1995). Nonsphericity of dust-like tropospheric aerosols: Implications for aerosol remote sensing and climate modeling. *Geophysical Research Letters*, *22*, 1077–1080. <https://doi.org/10.1029/95GL00798>
- Mishchenko, M. I., Travis, L. D., Kahn, R. A., & West, R. A. (1997). Modeling phase functions for dustlike tropospheric aerosols using a shape mixture of randomly oriented polydisperse spheroids. *Journal of Geophysical Research*, *102*(D14), 16,831–16,847. <https://doi.org/10.1029/96JD02110>
- Mishchenko, M. I., & Yurkin, M. A. (2017). On the concept of random orientation in far-field electromagnetic scattering by nonspherical particles. *Optics Letters*, *42*, 494–497.
- Muinsonen, K., Nousiainen, T., Fast, P., Lumme, K., & Peltoniemi, J. I. (1996). Light scattering by Gaussian random particles: Ray optics approximation. *Journal of Quantitative Spectroscopy and Radiative Transfer*, *55*(5), 577–601.
- Muñoz, O., Moreno, F., Guirado, D., Dabrowska, D. D., Volten, H., & Hovenier, J. W. (2012). The Amsterdam-Granada Light Scattering Database. *Journal of Quantitative Spectroscopy and Radiative Transfer*, *113*, 566–574.
- Muñoz, O., Volten, H., de Haan, J., Vassen, W., & Hovenier, J. W. (2001). Experimental determination of scattering matrices of randomly oriented fly ash and clay particles at 442 and 633 nm. *Journal of Geophysical Research*, *106*(D19), 22,833–22,844. <https://doi.org/10.1029/2000JD000164>
- Muñoz, O., Volten, H., de Haan, J. F., Vassen, W., & Hovenier, J. W. (2000). Experimental determination of scattering matrices of olivine and Allende meteorite particles. *Astronomy and Astrophysics*, *360*, 777–788.
- Muñoz, O., Volten, H., Hovenier, J. W., Beihelmann, B., van der Zande, W. J., Waters, L. B. F. M., & Rose, W. I. (2004). Scattering matrices of volcanic ash particles of Mount St. Helens, Redoubt, and Mount Spurr volcanoes. *Journal of Geophysical Research*, *109*, D16201. <https://doi.org/10.1029/2004JD004684>
- Nousiainen, T. (2009). Optical modeling of mineral dust particles: A review. *Journal of Quantitative Spectroscopy and Radiative Transfer*, *110*(14–16), 1261–1279.
- Nousiainen, T., Kahnert, M., & Lindqvist, H. (2011). Can particle shape information be retrieved from light-scattering observations using spheroidal model particles? *Journal of Quantitative Spectroscopy and Radiative Transfer*, *112*(13), 2213–2225.
- Nousiainen, T., & Vermeulen, K. (2003). Comparison of measured single-scattering matrix of feldspar particles with T-matrix simulations using spheroids. *Journal of Quantitative Spectroscopy and Radiative Transfer*, *79*–80, 1031–1042.
- Okada, K., Heintzenberg, J., Kai, K., & Qin, Y. (2001). Shape of atmospheric mineral particles collected in three Chinese arid-regions. *Geophysical Research Letters*, *28*, 3123–3126.
- Otto, S., Bierwirth, E., Weinzierl, B., Kandler, K., Esselborn, M., Tesche, M., et al. (2008). Solar radiative effects of a Saharan dust plume observed during SAMUM assuming spheroidal model particles. *Tellus Series B: Chemical and Physical Meteorology*, *61*, 270–296.
- Prospero, J. M., Ginoux, P., Torres, O., Nicholson, S. E., & Gill, T. E. (2002). Environmental characterization of global sources of atmospheric soil dust identified with the Nimbus 7 Total Ozone Mapping Spectrometer (TOMS) absorbing aerosol product. *Reviews of Geophysics*, *40*(1), 1002. <https://doi.org/10.1029/2000RG000095>
- Ramanathan, V., Crutzen, P. J., Kiehl, J. T., & Rosenfeld, D. (2001). Aerosols, climate, and the hydrological cycle. *Science*, *294*, 2119–2124.
- Reid, E. A., Reid, J. S., Meier, M. M., Dunlap, M. R., Cliff, S. S., Broumas, A., et al. (2003). Characterization of African dust transported to Puerto Rico by individual particle and size segregated bulk analysis. *Journal of Geophysical Research*, *108*(D19), 8591. <https://doi.org/10.1029/2002JD002935>
- Sinyuk, A., Torres, O., & Dubovik, O. (2003). Combined use of satellite and surface observations to infer the imaginary part of refractive index of Saharan dust. *Geophysical Research Letters*, *30*(2), 1081. <https://doi.org/10.1029/2002GL016189>
- Tegen, I., & Fung, I. (1994). Modelling of mineral dust in the atmosphere: Sources, transport, and optical thickness. *Journal of Geophysical Research*, *99*(D11), 22,897–22,914.
- Tegen, I., Lacis, A. A., & Fung, I. (1996). The influence on climate forcing of mineral aerosols from disturbed soils. *Nature*, *380*(6573), 419–422.
- van de Hulst, H. C. (1981). *Light scattering by small particles*. New York: Dover.
- Veghte, D. P., & Freedman, M. A. (2014). Facile method for determining the aspect ratios of mineral dust aerosol by electron microscopy. *Aerosol Science and Technology*, *48*(7), 715–724.
- Veihelmann, B., Nousiainen, T., Kahnert, M., & van der Zande, W. J. (2006). Light scattering by small feldspar particles simulated using the Gaussian random sphere geometry. *Journal of Quantitative Spectroscopy and Radiative Transfer*, *100*(1–3), 393–405.
- Veselovskii, I., Dubovik, O., Kolgotin, A., Lapyonok, T., DiGirolamo, P., Summa, D., et al. (2010). Application of randomly oriented spheroids for retrieval of dust particle parameters from multiwavelength lidar measurements. *Journal of Geophysical Research*, *115*, D21203. <https://doi.org/10.1029/2010JD014139>
- Volten, H., Muñoz, O., Hovenier, J. W., Rietmeijer, F. J. M., Nuth, J. A., Waters, L. B. F. M., & van der Zande, W. J. (2007). Experimental light scattering by fluffy aggregates of magnesiosilica, ferrosilica, and alumina cosmic dust analogs. *Astronomy and Astrophysics*, *470*, 377–386.
- Volten, H., Muñoz, O., Hovenier, J. W., & Waters, L. B. F. M. (2006). An update of the Amsterdam Light Scattering Database. *Journal of Quantitative Spectroscopy and Radiative Transfer*, *100*, 437–443.
- Volten, H., Muñoz, O., Rol, E., de Haan, J. F., Vassen, W., & Hovenier, J. W. (2000). Scattering matrices of mineral aerosol particles at 441.6 nm and 632.8 nm. *Journal of Geophysical Research*, *106*, 17,375–17,401. <https://doi.org/10.1029/2001JD900068>
- Wagner, S. C., Govaerts, Y. M., & Lattanzio, A. (2010). Joint retrieval of surface reflectance and aerosol optical depth from MSG/SEVIRI observations with an optimal estimation approach: 2. Implementation and evaluation. *Journal of Geophysical Research*, *115*, D02204. <https://doi.org/10.1029/2009JD011780>
- Wang, Y., Chakrabarti, A., & Sorensen, C. M. (2015). A light-scattering study of the scattering matrix elements of Arizona Road Dust. *Journal of Quantitative Spectroscopy and Radiative Transfer*, *163*, 72–79.
- Wriedt, T. (2002). Using the T-matrix method for light scattering computations by non-axisymmetric particles: Superellipsoids and realistically shaped particles. *Particle and Particle Systems Characterization*, *19*, 256–268.
- Yang, P., Feng, Q., Hong, G., Kattawar, G. W., Wiscombe, W. J., Mishchenko, M. I., et al. (2007). Modeling of the scattering and radiative properties of non-spherical dust-like aerosols. *Journal of Aerosol Science*, *38*(10), 995–1014. <https://doi.org/10.1016/j.jaerosci.2007.07.001>
- Yang, P., & Liou, K. N. (1996). Geometric-optics-integral-equation method for light scattering by non-spherical ice crystals. *Applied Optics*, *35*(33), 6568–6584.

- Yang, P., Liou, K. N., Mishchenko, M. I., & Gao, B. C. (2000). Efficient finite-difference time-domain scheme for light scattering by dielectric particles: Application to aerosols. *Applied Optics*, *39*(21), 3727–3737.
- Zubko, E., Muinonen, K., Muñoz, O., Nousiainen, T., Shkuratov, Y., Sun, W., & Videen, V. (2013). Light scattering by feldspar particles: Comparison of model agglomerate debris particles with laboratory samples. *Journal of Quantitative Spectroscopy and Radiative Transfer*, *131*, 175–187.